

Black Hole Interior and Time-like Entanglement Entropy

Zi-Hao Li, Run-Qiu Yang

Center for Joint Quantum Studies and Department of Physics, School of Science, Tianjin University, Yaguan Road 135, Jinnan District, 300350 Tianjin, P. R. China

E-mail: lieaction.lzh@gmail.com, aqiu@tju.edu.cn

ABSTRACT: We establish time-like entanglement entropy (TEE) as a novel tool to characterize the black hole interior from a single-boundary perspective. In the Schwarzschild-AdS black hole, we show that TEE of time-like boundary strips exhibits linear growth as a function of temporal width in the limit of large temporal width, and that its imaginary part carries physical significance rather than being a constant. By analyzing charged, scalar-hairy black holes, we present evidence that TEE detects a hidden “causal phase transition” separating Type-I and Type-II interiors — distinguished by singularity structure. We identify a critical temporal width τ_c that acts as the order parameter for this transition: for strips narrower than τ_c , the system enters a distinct “time-like entanglement phase” dominated purely by time-like contributions, up to a regulator effect; conversely, for strips wider than τ_c , space-like entanglement re-emerges. Notably, the existence of a Cauchy horizon drives the τ_c to infinity, leading to pure time-like entanglement. These results suggest that the TEE may supply a novel boundary quantum-information measure to detect structure hidden inside the black hole and suggests a deep connection between TEE and cosmic censorship.

Contents

1	Introduction	1
2	Time-like Entanglement Entropy in Schwarzschild-AdS Black Hole	4
2.1	Setup	5
2.2	Minimal Geometric Configuration of Schwarzschild-AdS Black Hole	7
2.3	Real and Imaginary Part	12
2.3.1	Real part	12
2.3.2	Imaginary part	13
2.4	Asymptotic Analysis for Large Temporal Width	15
3	Time-like Entanglement in Hairy Black Holes	16
3.1	Classifying Black Hole Interiors	17
3.1.1	Type-I/II spacetimes	17
3.1.2	The Type-II interior from holography	20
3.2	Time-like Entanglement Phase in Type-II Spacetimes	21
3.3	Phase Transition of Time-like Entanglement	24
4	Discussion	32
A	Uniqueness of the Minimal Area Configuration	33
B	Asymptotic Details of Null Limit	35

1 Introduction

The interior of a black hole presents a fundamental challenge to our understanding of gravity and spacetime. Unlike the exterior, the interior has unique features, notably a singularity where classical gravity breaks down. Many black hole solutions, such as the Reissner-Nordström (RN) and Kerr spacetimes, also have an inner Cauchy horizon behind the event horizon. Efforts to understand the interior have yielded important insights. For example, the work of Belinski, Khalatnikov, and Lifshitz (BKL) shows that the approach to certain space-like singularities can exhibit chaotic behavior [1–3]. More recent studies have demonstrated that the Cauchy horizon in certain charged black holes becomes non-linearly unstable, particularly in the presence of scalar hair [4, 5].

Despite these theoretical advances, the relationship between the black hole interior and its outside is not fully understood. However, the holographic duality offers a powerful new toolkit. The anti-de Sitter/conformal field theory correspondence (AdS/CFT) claims that the physics of a bulk spacetime in an asymptotically anti-de Sitter (AdS) spacetime is

equivalent to a conformal field theory (CFT) on the spacetime boundary [6–8]. Specifically, the duality between an eternal AdS black hole and two entangled boundary theories provides a concrete framework where the black hole interior is encoded in the entanglement structure of two boundaries [9, 10]. Within this framework, a hierarchy of probes have emerged, yet each comes with limitations. On one hand, “weak” probes can capture data behind the event horizon but are fundamentally incapable of reaching the singularity. Standard Holographic Entanglement Entropy (HEE), governed by the Ryu-Takayanagi prescription [11, 12], and the Complexity=Volume (CV) conjecture [13] fall into this category. Their geometric duals, space-like minimal surfaces and maximal volumes, respectively, cannot reach the space-like singularity in general dimensions [14, 15], thus providing only a partial picture of the interior geometry¹. On the other hand, “strong” probes do exist that can reach the singularity, and they have yielded profound insights into the black hole interior. For instance, the geodesic approximation to two-sided correlation functions has been used to probe the near-singularity geometry [15, 16]. The Complexity = Action (CA) conjecture, through the evaluation of the action on the Wheeler- DeWitt patch, provides another powerful tool to track the geometry deep inside the horizon [17, 18]. However, the probes capable of reaching the singularity typically rely on correlation data from two disconnected boundaries. This leaves us with a critical dilemma: the tools that are single-sided (such as HEE) cannot probe the singularity, and the tools that can probe the singularity (such as CA conjecture) are not single-sided.

Particularly, focusing on entanglement entropy, this fundamental limitation raises a natural question: can this barrier be overcome by considering a different class of entanglement? Such a candidate has recently emerged in the form of Time-like Entanglement Entropy (TEE) [19], a generalization of HEE to *time-like* separated boundary regions, which belongs to the class of *single-sided* observables. The concept of entanglement entropy for time-like subregion was originally proposed in early holographic studies [20], where it was proposed to resolve the asymmetry between finite-size and finite-temperature corrections in $T\bar{T}$ deformed CFTs². TEE is particularly sensitive to the deep interior structure of a black hole. This is because its geometric dual, unlike that of HEE, can directly reach the singularity [22–25]. This property makes TEE a rare boundary observable that able to directly probe the near-singularity structure of a black hole. Consequently, TEE opens a new window to investigate the physics of the black hole interior and its singularity through the behavior of a boundary quantity.

The study of TEE is a rapidly developing field, with several computational frameworks proposed in recent years. These approaches which are base on boundary field perspective, include operator-algebraic definition of TEE as a real-valued quantity derived from space-like entanglement [26], boundary field theory techniques utilizing the real-time Schwinger-Keldysh formalism [27, 28] and imaginary time replica method [29, 30] and frameworks using non-hermitian density matrices in quantum many-body systems [31]. From the bulk

¹Only in lower-dimensional cases, such as $d = 1$ or $d = 2$ (BTZ black hole case), where the surfaces reduce into geodesics, can HEE and CV probes access the full interior up to the singularity. However, these are exceptional cases and do not represent the generic behavior in higher dimensions, which is the focus of our investigation.

²The asymmetry is further examined in this specific context in [21].

perspective, progress has been made using top-down holographic models derived from string backgrounds [32, 33], a framework deriving the TEE from the Rindler method [34, 35], equations of motion for extremal surfaces in non-conformal and non-relativistic settings [36, 37], and calculations involving complex bulk geometries of extremal surfaces [38, 39]. Among these candidates, the proposal which constructs the geometric dual from piece-wise smooth space-like and time-like segments, known as the Complex-valued Weak Extremal Surface (CWES) prescription [19, 23, 24], is particularly powerful for probing the black hole interior directly without analytic continuation.

Equipped with these geometric tools, pioneering studies have begun to explore black hole interiors. For instance, properties of TEE, captured by space-like and time-like geodesics, have been used to gain insights into the interiors of lower-dimensional spacetimes [29, 40]. Similarly, in $2 + 1$ -dimensional black holes, TEE has been shown to serve as a preliminary probe of the singularity [41]. However, these initial applications have largely focused on simpler models. The relationship between the interior geometry of higher-dimensional black holes with complex internal structures and the boundary field theory remains a crucial and largely unexplored question.

In this paper, we employ the CWES/TEE framework [19, 23, 24] to demonstrate that time-like entanglement entropy (TEE) provides a sharp probe for a crucial dichotomy in the causal nature of singularities, one that earlier studies found using two-sided probes requiring entanglement data from two boundaries [15, 42, 43]. We frame this classification in terms of two classes, which we call *Type-I* and *Type-II*, distinguished by their interior causal structure. This geometric distinction is rooted in the causal shape of the interior in the Penrose diagram, with Type-I spacetimes featuring “concave” or “flat” space-like singularities and Type-II spacetimes possessing “convex” ones, leading to markedly different causal behavior inside the black hole. Standard holographic observables (for example, holographic entanglement entropy and thermodynamic observables) are insensitive to this distinction because they probe the geometry only down to the event horizon. By contrast, TEE can see deep interior changes, thus revealing a dramatic transition: Type-II interiors exhibit what we term a “time-like phase” for boundary time-like strips. When the temporal width is sufficiently narrow, the entanglement is dominated by time-like contributions and the space-like segments of extremal surface is reduced to the UV regulator contributions. This regulator effect stems from the existence of both a spatial and a temporal minimal resolution scale, which arises in the limit where a space-like extremal surface approaches a null hypersurface. We identify the upper bound of this time-like dominated regime, the critical temporal width τ_c , as a physically intuitive order parameter. Only the Type-II spacetime admits a nonzero τ_c . The emergence of a non-zero “time-like entanglement gap” ($\tau_c > 0$) thus provides a clear boundary signature of hidden interior transitions, effectively “hearing” the shape of the singularity from the outside. While other two-sided probes (e.g., Complexity=Action) may also partly respond to this phenomenon [15, 42, 43], our central contribution is to establish TEE as a novel, single-sided diagnostic of the hidden causal phase.

The organization of this paper is as follows. In Sec. 2 we present a detailed calculation for the Schwarzschild-AdS black hole. This not only validates our methodology and estab-

lishes the benchmark Type-I behavior, where the order parameter τ_c vanishes identically, but also reveals that the linear growth in the limit of large temporal width and the imaginary part of TEE cannot be absorbed into the usual UV spatial cutoff and therefore carries physical information. In Sec. 3 we construct Type-II interiors using a backreacting holographic superconductor, trace the transition from Type-II to Type-I as temperature varies, and show that a nonzero τ_c serves as the order parameter, exploring the rich phenomenology associated with its emergence. Notably, we show that the existence of a Cauchy horizon drives τ_c to infinity, resulting in a state of pure time-like entanglement. Finally, in Sec. 4, we summarize our findings, discuss their implications and outline open questions.

2 Time-like Entanglement Entropy in Schwarzschild-AdS Black Hole

Before exploring the rich interior structures of complex black holes, it is instructive to first apply the TEE framework to the simplest, non-trivial example: the Schwarzschild-AdS black hole (SAdS). This black hole, with its simple interior lacking inner horizons or hair, offers a controlled setting to develop our methods. It thereby establishes a baseline against which the novel phenomena in more complex spacetimes (Sec. 3) can be clearly contrasted and understood.

Our starting point is the metric for a $D = (d + 1)$ -dimensional SAdS black hole, which in Schwarzschild coordinates is given by³:

$$\begin{aligned} ds^2 &= -f(r) dt^2 + \frac{dr^2}{f(r)} + r^2 d\Sigma_{k,d-1}^2, \\ f(r) &= k - \frac{\omega^{d-2}}{r^{d-2}} + \frac{r^2}{\ell_{\text{AdS}}^2}. \end{aligned} \tag{2.1}$$

Here, ℓ_{AdS} denotes the AdS radius, while $k = \{+1, 0, -1\}$ describes the curvature of the $(d - 1)$ -dimensional spatial section $d\Sigma_{k,d-1}^2$, which is given by

$$d\Sigma_{k,d-1}^2 = \begin{cases} d\theta^2 + \sin^2 \theta d\Omega_{d-2}^2, & \text{for } k = +1; \\ dx^2 + dy_{d-2}^2, & \text{for } k = 0; \\ d\sigma^2 + \sinh^2 \sigma d\Omega_{d-2}^2, & \text{for } k = -1. \end{cases} \tag{2.2}$$

For simplicity, and to connect with holographic applications, we will focus on the planar case throughout this paper, i.e., we set $k = 0$ in Eqs. (2.1) and (2.2). The horizon radius r_h is defined as the largest real root of the equation $f(r_h) = 0$, which relates it to the ‘mass’ parameter ω

$$k - \frac{\omega^{d-2}}{r_h^{d-2}} + \frac{r_h^2}{\ell_{\text{AdS}}^2} = 0. \tag{2.3}$$

This spacetime is static, admitting the time-like Killing vector field $\xi^\mu = \partial_t$.

³Here we have assumed the spatial dimension of bulk spacetime satisfies $d > 2$. The case of BTZ black hole with $d = 2$ is reduced to the situation discussed in Ref. [23]. Our result about the imaginary part of TEE (2.37) for $d = 2$ in this paper is consistent with Ref. [23].

2.1 Setup

Having defined the spacetime geometry, our goal is to compute the TEE for a specific boundary subregion within this background. To do so, we will employ the Complex-valued Weak Extremal Surface (CWES) prescription introduced in Ref. [19, 23, 24]. This prescription instructs us to find a special, piece-wise smooth, codimension-2 surface $\Gamma_{\mathcal{T}}$ in the bulk. The surface $\Gamma_{\mathcal{T}}$ is anchored on the boundary subregion of interest, \mathcal{T} , and its area holographically computes the TEE as follows

$$S_{\mathcal{T}} = \text{Min} \left\{ \text{Ext} \frac{\mathcal{A}(\Gamma_{\mathcal{T}})}{\partial \Gamma_{\mathcal{T}} 4G_N^{(d+1)}} \right\}. \quad (2.4)$$

Here, $\mathcal{A}(\Gamma_{\mathcal{T}})$ corresponds to the complex-valued area of the piece-wise smooth surface $\Gamma_{\mathcal{T}}$. The operations ‘‘Ext’’ and ‘‘Min’’ signify that we must find a surface that is both extremal (its area is stationary under local deformations) and minimal among all such valid candidates, according to the ordering relation ‘‘ \prec ’’ (or ‘‘ \succ ’’) defined by [23]. The power of this prescription lies in the unique structure of $\Gamma_{\mathcal{T}}$: it is composed of both space-like and time-like extremal segments, pieced together smoothly, which allows the surface to penetrate the deep interior and reach the singularity, which is impossible for the purely space-like subregions used to compute standard HEE.

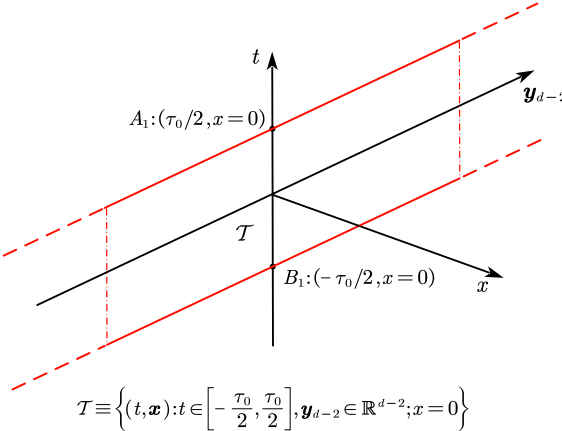


Figure 1: A schematic diagram of time-like strip (depicted in red) on the boundary. Here the boundary is d -dimensional and spanned by coordinates $\{t, x, \mathbf{y}_{d-2}\}$ with $\mathbf{y}_{d-2} \in \mathbb{R}^{d-2}$. This strip-configuration serves as the geometric generalization of a time-like interval in higher dimensions.

To apply this prescription, we must first specify the boundary subregion \mathcal{T} . In higher dimensions, we consider a time-like ‘‘strip’’ of temporal width τ_0 , extending infinitely in $d-2$ spatial directions,

$$\mathcal{T} \equiv \left\{ (t, \mathbf{x}) : t \in \left[-\frac{\tau_0}{2}, \frac{\tau_0}{2} \right], \mathbf{y}_{d-2} \in \mathbb{R}^{d-2}; x = 0 \right\}, \quad (2.5)$$

as depicted in Fig. 1. The endpoints of time-like strip \mathcal{T} on boundary CFT_d are denoted by A_1 and B_1 with the time coordinate $t = \pm \frac{\tau_0}{2}$ (note that for $d = 2$, this strip-configuration

reduces to a time-like interval usually considered in the literature, such as [23, 40, 41]). Our task is now clear: find the minimal CWES anchored on this strip \mathcal{T} and evaluate its area.

With this setup, there are two relevant segment-smooth surfaces that could touch the singularity within the black hole interior, shown in Fig. 2(a), one of which is $A_1A_2B_2B_1$ and the other is $A_1B_2A_2B_1$. Applying arguments analogous to the “triangle inequality” for spatial extremal surfaces, and defining $\mathcal{A} = \mathcal{A}/\mathcal{V}_{d-2}$ as the complex valued area density (where $\mathcal{V}_{d-2} \equiv \int d^{d-2}y$ is the transverse volume of the boundary strip)⁴, we have

$$\begin{aligned}\mathcal{A}(A_1A_2) &< \mathcal{A}(A_1D) + \mathcal{A}(DA_2) , \\ \mathcal{A}(B_1B_2) &< \mathcal{A}(B_1D) + \mathcal{A}(DB_2) ; \\ \mathcal{A}(A_1A_2B_2B_1) &\prec \mathcal{A}(A_1B_2A_2B_1) .\end{aligned}\tag{2.6}$$

Here “ \prec ” in last line denotes the ordering relationship defined in Ref. [23] to obtain the minimal CWES.

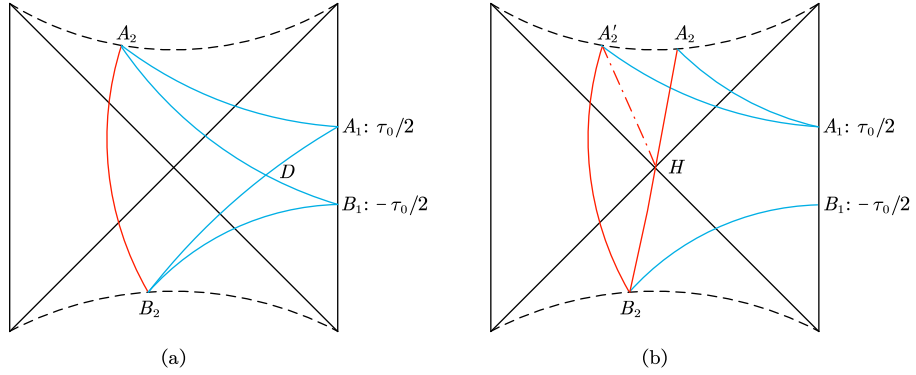


Figure 2: Configurations of CWES of time-like strip in SAdS black hole. Blue lines stand for space-like surface and green lines represent time-like surface. (a) There are two types of relevant configurations of CWESs, which are $A_1A_2B_2B_1$ and $A_1B_2A_2B_1$. (b) Comparison of time-like paths: The symmetric surface A_2B_2 passes through the bifurcation surface H of the event horizon, whereas A'_2B_2 represents a generic path.

Consequently, we only need to consider the segment-smooth surface $A_1A_2B_2B_1$ of Fig. 2(a), which is related to two different cases, “non-crossing” configuration $A_1A'_2B_2B_1$ and “crossing” configuration $A_1A_2B_2B_1$ shown in Fig. 2(b). The red solid straight line A_2B_2 stands for the time-like surface passing through the bifurcation surface H of event horizon, while A'_2B_2 represents a general time-like surface connecting the points of past and future singularity. Let A'_2H denote the time-like segment connecting A'_2 and H . Since time-like surfaces obey the “anti-triangle inequality”, we then find

$$\mathcal{A}(A'_2B_2) \succ \mathcal{A}(A'_2H) + \mathcal{A}(HB_2) .\tag{2.7}$$

⁴Here we work with the area density \mathcal{A} to replace the area \mathcal{A} , because the total area is trivially infinite due to the infinite transverse volume of the boundary strip for $\mathbf{y}_{d-2} \in \mathbb{R}^{d-2}$.

Furthermore, the time translation symmetry of SAdS black hole (generated by the Killing vector ∂_t) implies that $\mathcal{A}(A'_2 H) = \mathcal{A}(A_2 H)$. Combining these relations, we obtain:

$$\mathcal{A}(A_1 A_2 B_2 B_1) \prec \mathcal{A}(A_1 A'_2 B_2 B_1) . \quad (2.8)$$

This result confirms that, to find the minimal CWES and compute the TEE in the SAdS black hole, it suffices to study the configuration where the time-like segment passes through the bifurcation surface, as depicted by the segment-smooth surface $A_1 A_2 B_2 B_1$ in Fig. 2(b).

2.2 Minimal Geometric Configuration of Schwarzschild-AdS Black Hole

To describe the surfaces $A_1 A_2$ and $B_1 B_2$, which smoothly cross the event horizon and terminate at the singularity ($r = 0$), the standard Schwarzschild coordinates (2.1) are inadequate due to the coordinate singularity at the horizon. We therefore switch to ingoing and outgoing Eddington coordinates for segments $A_1 A_2$ and $B_1 B_2$ respectively by defining:

$$\begin{aligned} v &= t + r_* = t + \int_{\infty}^r \frac{d\tilde{r}}{f(\tilde{r})} , \\ u &= t - r_* = t - \int_{\infty}^r \frac{d\tilde{r}}{f(\tilde{r})} . \end{aligned} \quad (2.9)$$

Accordingly, we utilize the metrics adapted to these respective coordinate patches (ingoing and outgoing):

$$\begin{aligned} ds^2 &= -f(r) dv^2 + 2dvdr + r^2 (dx^2 + dy_{d-2}^2) , \\ ds^2 &= -f(r) du^2 - 2dudr + r^2 (dx^2 + dy_{d-2}^2) ; \end{aligned} \quad (2.10)$$

and in this coordinate system, the metric behaves regularly across the horizon $r = r_h$.

In Eddington coordinates (2.10), we parameterize the endpoints at the singularity of the segment-smooth surface $A_1 A_2 B_2 B_1$ as $A_2 : (v_{A_2}, \dots)$ and $B_2 : (u_{B_2}, \dots)$ respectively, as illustrated in Fig. 3(a). Here the ‘‘endpoints’’ A_2 and B_2 are related to each other so that the time-like extremal surface passes through the bifurcated surface of event horizon. This leads to two important results. First, the area contribution from the time-like segment $A_2 B_2$ is independent of the boundary temporal width τ_0 (see Sec. 2.3.2 for analytic result). Therefore, for the extremization problem, we treat the area of $A_2 B_2$ as a constant and focus on minimizing the contribution from the space-like segments $A_1 A_2$ and $B_2 B_1$. Second, constraint from $A_2 B_2$ requires that the t -coordinates of A_2 and B_2 are the same, i.e., $t|_{A_2} = t|_{B_2}$. In other words, the time-like surface $A_2 B_2$ acts as a geometric constraint, fixing the Schwarzschild coordinate time of the space-like surfaces $A_1 A_2$ and $B_2 B_1$ at the singularity. As a result, Eddington coordinate time v_{A_2} and u_{B_2} at the singularity are not independent. This reduces the variational problem to a single independent parameter, which we choose to be v_{A_2} for the following analysis. As depicted in Fig. 3(a), varying v_{A_2} generates a family of candidate extremal surfaces. Our task is therefore reduced to find the specific v_{A_2} that corresponds to the minimal CWES, i.e., the physical configuration with the minimal extremal area among all candidate configurations.

To identify this minimal configuration, our analysis proceeds in two main steps. First, we will express the real part of the CWES area $\mathcal{A}(A_1 A_2 B_2 B_1)$ as a function of the endpoint

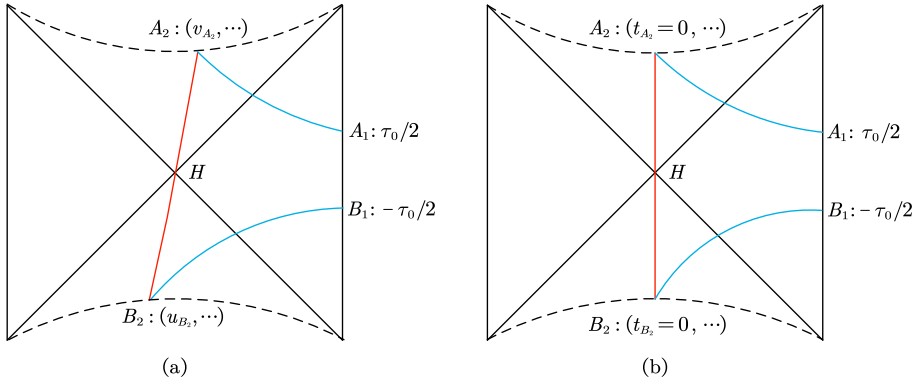


Figure 3: (a) The real part of the CWES area density plotted as a function of the endpoint parameter v_{A_2} , where varying this parameter generates a family of candidate extremal surfaces. (b) The minimal extremal configuration of CWES, corresponding to the time-symmetric case $t|_{A_2} = t|_{B_2} = 0$.

parameter v_{A_2} , thereby reducing the problem to a one-variable extremization problem. Second, we will utilize the Hamilton-Jacobi formalism to derive the general condition satisfied by any extremal surface. This condition reveals an intuitive solution: the time-symmetric “vertical” configuration (corresponding to $t|_{A_2} = t|_{B_2} = 0$, see Fig. 3(b)), which we subsequently demonstrate to be the unique solution. The details of each step are presented below.

(1) **Expressing the Area via a Conserved Quantity.** Our first step is to find an expression for the area of the space-like surfaces, $\mathcal{A}_{A_1 A_2}$ and $\mathcal{A}_{B_1 B_2}$, as a function of the endpoint coordinate v_{A_2} .

In Eddington coordinates (2.10), we can parameterize the extremal surface by $\{v, r = r(v), x = 0, \mathbf{y}_{d-2} \in \mathbb{R}^{d-2}\}$, subject to the boundary conditions $r(\tau_0/2) \rightarrow \infty$ and $r(v_{A_2}) = 0$. The area density functional $\mathcal{A}_{A_1 A_2}$ for the segment $A_1 A_2$ is then given by the integral of the Lagrangian functional L :

$$\mathcal{A}_{A_1 A_2} = \int_{v_{A_2}}^{\tau_0/2} dv L(r, r') , \quad (2.11)$$

$$L(r, r') = r^{d-2} (v) \sqrt{-f(r) + 2r'} ,$$

where $r' \equiv \frac{dr}{dv}$. Crucially, the SAdS metric is static, meaning the Lagrangian L has no explicit dependence on the “time” coordinate v . We could find an associated conserved quantity along the extremal surface $E = r' \frac{\partial L}{\partial r'} - L$,

$$E = \frac{r^{d-2} (f(r) - r')}{\sqrt{-f(r) + 2r'}} \equiv H_*^2 . \quad (2.12)$$

Here H_* is assumed to be a real constant. The equation of motion for the surface can now

be solved for r' in terms of r and the constant H_* . We obtain the following equation from⁵ Eq. (2.12) for surface A_1A_2

$$r' = r^{4-2d} X (X + H_*^2) , \quad (2.13)$$

where we have introduced $X = \sqrt{H_*^4 + r^{2d-4} f(r)}$. Notice that when $f(r) < 0$ (inside the horizon) and $|f(r)|$ is large enough, term $H_*^4 + r^{2d-4} f(r)$ in the root $\sqrt{H_*^4 + r^{2d-4} f(r)}$ may become negative, preventing a real square root. This effectively limits the domain of existence for H_* . The condition for a real-valued solution is that H_* must have a lower bound $H_*^4 \geq -\max\{r^{2d-4} f(r)\}$. For SAdS case, we have

$$H_{*,\min} = G^{1/4}(r_c) , \quad (2.14)$$

where $G(r) = \omega^{d-2} r^{d-2} - r^{2d-2} / \ell_{\text{AdS}}^2$ and $r_c = [(d-2)\omega^{d-2} \ell_{\text{AdS}}^2 / (2d-2)]^{1/d}$ is the critical point where $G(r)$ reaches its extremum. The critical point r_c derived here signifies that the space-like extremal surface A_1A_2 , which connects the boundary to the singularity, approaches a critical extremal surface located at $r = r_c$. The surface A_1A_2 lingers at this critical extremal surface for an arbitrarily long time, which, as we will demonstrate both numerically (Fig. 6(a)) and analytically (Eq. (2.41)) in Sec. 2.4, corresponds precisely to the large boundary temporal width⁶ $\tau_0 \rightarrow \infty$.

For the surface A_1A_2 , we fix the boundary time at $v = \tau_0/2$ at A_1 . The boundary conditions for the extremal surface are thus given by

$$A_1 : (r = +\infty, v = \tau_0/2) , \quad A_2 : (r = 0, v = v_{A_2}) . \quad (2.15)$$

The relationship between constant H_* and the time difference $\tau_0/2 - v_{A_2}$ is determined by integrating with respect to $dv = dr/r'$

$$+\frac{\tau_0}{2} - v_{A_2} = \int_{r=0}^{r=+\infty} \frac{dr}{r^{4-2d} X (X + H_*^2)} . \quad (2.16)$$

With the conserved quantity H_* implicitly fixed by the above equation, the on-shell area functional of the surface A_1A_2 can be expressed as $\mathcal{F}(\tau_0, v_{A_2})$, defined by the radial integral:

$$\mathcal{F}(\tau_0, v_{A_2}) \equiv \int_{v_{A_2}}^{\tau_0/2} dv \frac{r^{2d-4}(v)}{H_*^2} (f(r) - r') = \int_{r=0}^{r=+\infty} dr \frac{r^{2d-4}}{X} . \quad (2.17)$$

Here $X = \sqrt{H_*^4 + r^{2d-4} f(r)}$ and $\mathcal{F}(\tau_0, v_{A_2})$ is the ‘‘on-shell’’ value of area integration (2.11). Note that in this expression, H_* is treated as a function of the v_{A_2} and τ_0 via Eq. (2.16).

For the other surface B_1B_2 , which originates at the boundary B_1 with $r(-\tau_0/2) \rightarrow \infty$ and ends at a singularity point B_2 with $r(u_{B_2}) = 0$, one could repeat the above procedure

⁵Directly solving for r' from Eq. (2.12) leads to $r' = r^{4-2d} X (X \pm H_*^2)$. Here, only the positive branch ‘‘+’’ is admissible because the negative sign would imply $r' = 0$ at the horizon, which is physically invalid.

⁶The phenomenon that a critical extremal surface governs the behavior of TEE in the limit of large temporal width is analogous to that observed in the context of space-like entanglement entropy [14, 44] and complexity [45]. Furthermore, Ref. [38] also identified such a critical surface controlling the behavior of complex bulk extremal surfaces in the large τ_0 regime in the context of TEE, following a proposal different from this paper.

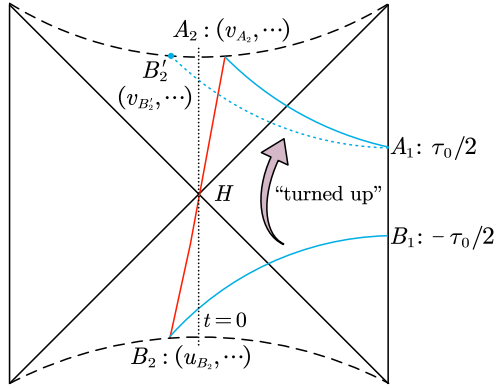


Figure 4: The surface $A_1B'_2$ corresponds to the “turned up” time-reversed image of surface B_1B_2 , where geometric constraint requires $t|_{B'_2} = -t|_{B_2} = -t|_{A_2}$.

in an analogous manner. However, a full recalculation is unnecessary due to the time-reversal symmetry of the SAdS spacetime ($t \rightarrow -t$, or equivalently $u \leftrightarrow -v$ in Eddington coordinates). Consequently, surface B_1B_2 can be mapped to a time-reversed mirror image, which we denote as the “turned up” surface $A_1B'_2$, as illustrated in Fig. 4. Similar to the surface A_1A_2 , this mirror surface $A_1B'_2$ is parameterized by ingoing Eddington coordinates (r, v, \dots) and is anchored to the same asymptotic boundary condition $A_1 : (r \rightarrow +\infty, v = \tau_0/2)$. However, its behavior at the singularity B'_2 is distinct. Governed by time-reversal symmetry and the geometric constraints of the time-like segment A_2B_2 , the Schwarzschild coordinate time at the singularity B'_2 satisfies the relation $t|_{B'_2} = -t|_{B_2}$. Combined with the condition $t|_{A_2} = t|_{B_2}$, this implies $t|_{B'_2} = -t|_{A_2}$. In terms of ingoing Eddington coordinates, this imposes a condition about the endpoints of A_1A_2 and $A_1B'_2$ at the singularity

$$v_{A_2} + v_{B'_2} = v_0 , \quad (2.18)$$

where we have defined the constant $v_0 \equiv 2 \int_{\infty}^0 \frac{d\tilde{r}}{f(\tilde{r})}$. Therefore, the area density $\mathcal{A}_{B_1B_2}(u_{B_2})$ can be identified with $\mathcal{A}_{A_1B'_2}(v_{B'_2})$, subject to the parameter shift $v_{B'_2} = v_0 - v_{A_2}$. This implies that $\mathcal{A}_{A_1B'_2}(v_{B'_2})$ is governed by the same functional form as $\mathcal{A}_{A_1A_2}(v_{A_2})$, but evaluated for a distinct shifted boundary condition

$$A_1 : (r = +\infty, v = \tau_0/2) , \quad B'_2 : \left(r = 0, v = v_{B'_2} = v_0 - v_{A_2} \right) . \quad (2.19)$$

Explicitly, for the surface $A_1B'_2$, the conserved quantity \tilde{H}_* is determined by:

$$+\frac{\tau_0}{2} - (v_0 - v_{A_2}) = \int_{r=0}^{r=+\infty} \frac{dr}{r^{4-2d} \tilde{X} \left(\tilde{X} + \tilde{H}_*^2 \right)} , \quad (2.20)$$

where $\tilde{X} = \sqrt{\tilde{H}_*^4 + r^{2d-4} f(r)}$. From this equation we can solve \tilde{H}_* for given v_{A_2} . The area of extremal surface then reads

$$\mathcal{A}_{A_1B'_2} = \int_{r=0}^{r=+\infty} dr \frac{r^{2d-4}}{\tilde{X}} . \quad (2.21)$$

Comparing Eqs. (2.20), (2.21) and Eqs. (2.16), (2.17), we can find

$$\mathcal{A}_{A_1B'_2} = \mathcal{F}(\tau_0, v_0 - v_{A_2}) , \quad (2.22)$$

and combining these results, the total real part of the CWES area is given by:

$$\mathcal{A}(A_1A_2B_2B_1) = \mathcal{A}_{A_1A_2} + \mathcal{A}_{A_1B'_2} = \mathcal{F}(\tau_0, v_{A_2}) + \mathcal{F}(\tau_0, v_0 - v_{A_2}) . \quad (2.23)$$

We have thus completed the first step: the area is expressed as a function $\mathcal{F}(x, y)$ via Eq. (2.17) and (2.16).

(2) Hamilton-Jacobi theory of extremal surface. With the area now expressed as a function of v_{A_2} (Step 1), we proceed to the second step: determining the condition that extremizes this area. For this task, the Hamilton-Jacobi formalism provides the most natural and powerful language, as it directly relates the variation of the on-shell action (here, the area density) with respect to the endpoint coordinates to the conserved quantities.

According to the Hamilton-Jacobi equation, the derivative of the action with respect to the “time” coordinate at the endpoint yields the negative of the conserved energy:

$$\frac{\partial \mathcal{A}_{A_1A_2}}{\partial v_{A_2}} = \frac{\partial \mathcal{F}(\tau_0, v_{A_2})}{\partial v_{A_2}} = -E(v_{A_2}) . \quad (2.24)$$

Similarly, for the second segment $A_1B'_2$, applying the chain rule to the shifted argument $v_0 - v_{A_2}$ we will obtain

$$\frac{\partial \mathcal{A}_{A_1B'_2}}{\partial v_{A_2}} = \frac{\partial \mathcal{F}(\tau_0, v_0 - v_{A_2})}{\partial v_{A_2}} = E(v_0 - v_{A_2}) . \quad (2.25)$$

For a given τ_0 , here the function E is defined according to Eq. (2.12). Thus, the variation of the total area is given by:

$$\frac{\partial \mathcal{A}_{A_1A_2B_2B_1}}{\partial v_{A_2}} = E(v_0 - v_{A_2}) - E(v_{A_2}) . \quad (2.26)$$

To determine the extremal value of total area $\mathcal{A}_{A_1A_2B_2B_1}$, we only need to impose the following stationarity equation

$$\frac{\partial \mathcal{A}_{A_1A_2B_2B_1}}{\partial v_{A_2}} = 0 , \quad (2.27)$$

which means a simple condition for the extremal configuration $E(v_{A_2}) = E(v_{B'_2} = v_0 - v_{A_2})$. A manifest solution to this condition is $v_{A_2} = v_{B'_2} = v_0 - v_{A_2}$, which corresponds to the perfectly symmetric “vertical” configuration $t|_{A_2} = t|_{B'_2} = t|_{B_2} = 0$, as illustrated in Fig. 3(b). In appendix A, we will show that $E(v_{A_2})$ is indeed strictly monotonic, which rigorously establishes that $v_{A_2} = v_0 - v_{A_2} \Leftrightarrow t|_{A_2} = t|_{B_2} = 0$ is the unique extremal solution.

Therefore, the minimal CWES configuration for a SAdS black hole is the time-symmetric “vertical” one shown in Fig. 3(b). This establishes a well-defined and unambiguous geometric dual for the TEE, allowing us to proceed with its analytical and numerical evaluation.

In summary, we can conclude that the CWES proposal is well-posed for SAdS black holes, where both the time-like and space-like extremal surfaces satisfy the extremal conditions. To obtain the TEE of SAdS case, we now only need to evaluate the area of this specific vertical configuration.

2.3 Real and Imaginary Part

The analysis in Sec. 2.2 rigorously established that the minimal CWES corresponds to the time-symmetric configuration ($t|_{A_2} = t|_{B_2} = 0$). This provides us with a well-defined geometric quantity to compute. We now proceed to evaluate its area, which consists of a real part from the two space-like segments A_1A_2 , B_1B_2 and an imaginary part from the time-like segment A_2B_2

$$\mathcal{A}(A_1A_2B_2B_1) = \text{Re}\mathcal{A}_{A_1B_1B_2A_2}(\tau_0) + i\text{Im}\mathcal{A}_{A_1B_1B_2A_2} . \quad (2.28)$$

2.3.1 Real part

With the condition $t|_{A_2} = t|_{B_2} = 0$, the relationships we derived in Eqs. (2.16) and (2.20) simplify significantly. The total boundary temporal width τ_0 and the total real area $\text{Re}\mathcal{A}$ can be expressed as integrals dependent on the conserved quantity H_* :

$$\tau_0(H_*) = 2 \int_{r=0}^{r=+\infty} dr \frac{r^{2d-4}}{X(X+H_*^2)} , \quad (2.29)$$

$$\text{Re}\mathcal{A}(H_*) = 2 \int_{r=0}^{r=+\infty} dr \frac{r^{2d-4}}{X} , \quad (2.30)$$

where, as before, $X = \sqrt{H_*^4 + r^{2d-4}f(r)}$.

Our objective is to determine the real part $\text{Re}\mathcal{A}(\tau_0)$. A direct approach would require inverting Eq. (2.29) to find $H_*(\tau_0)$ analytically and then substituting it into Eq. (2.30). However, the integral in Eq. (2.29) is highly non-trivial and cannot be inverted analytically in higher dimensions SAdS black hole. To overcome this challenge, we adopt a more powerful numerical strategy: we treat H_* as the fundamental independent parameter. By varying H_* starting from its allowed minimum value, $H_{*,\min}$, we can numerically compute a series of corresponding pairs $(\tau_0(H_*), \text{Re}\mathcal{A}(H_*))$. Plotting these pairs directly yields the desired functional relationship $\text{Re}\mathcal{A}(\tau_0)$ without the need for explicit inversion:

$$\begin{cases} \tau_0 = \tau_0(H_*) , \\ \text{Re}\mathcal{A} = \text{Re}\mathcal{A}(H_*) ; \end{cases} \iff \text{Re}\mathcal{A} = \text{Re}\mathcal{A}(\tau_0) . \quad (2.31)$$

Before calculating the real part of area density $\mathcal{A}(A_1A_2B_2B_1)$, we should notice that the entanglement entropy generally has a divergence when we integrate from $r = 0$ to $r = \infty$. This is a standard feature of holographic entanglement entropy, corresponding to the infinite entanglement of short-distance modes in the dual field theory. Thus in order to evaluate the finite, physical area from the integral (2.30), we employ the standard vacuum background subtraction scheme [11], subtracting the divergent area in pure AdS spacetime. The regularized area is given by:

$$\text{Re}\mathcal{A}_{\text{reg}} = \text{Re}\mathcal{A}_{\text{BH}} - \text{Re}\mathcal{A}_{\text{AdS}}^0 , \quad (2.32)$$

where $\text{Re}\mathcal{A}_{\text{AdS}}^0$ is the (also divergent) area in pure AdS spacetime, whose contribution is scheme-dependent but does not affect the universal features of the final result. Adopting a standard cutoff regularization, this term is given by [24]:

$$\text{Re}\mathcal{A}_{\text{AdS}}^0 = \frac{2}{d-2} \ell_{\text{AdS}}^{d-1} \epsilon_{\text{AdS}}^{2-d} , \quad (2.33)$$

where ϵ is a UV cutoff near the AdS boundary. Crucially, since the vacuum contribution is a constant (independent of the bulk path variation), this regularization scheme does not affect the extremization analysis or the stability of the solution derived in the previous section.

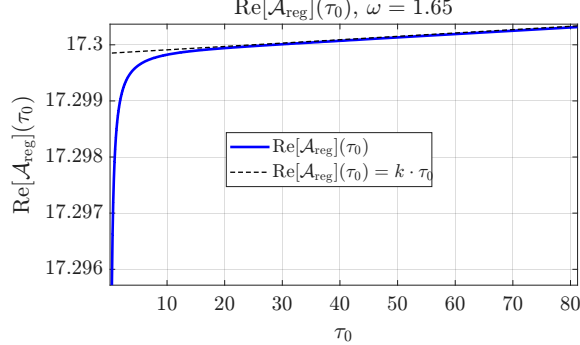


Figure 5: The regularized real part of the TEE $\text{Re}\mathcal{A}_{\text{reg}} = \text{Re}\mathcal{A}(\tau_0)$. The solid blue curve represents the full numerical result obtained by parametrically solving Eqs. (2.29) and (2.30). The dashed black line shows the theoretical linear asymptotic behavior for large τ_0 , $\text{Re}\mathcal{A} \approx k \cdot \tau_0$, as predicted in Eq. (2.43). The numerical curve is shown to converge perfectly to this theoretical line.

Under the subtraction scheme of Eq. (2.32), the final numerical result for the regularized real part $\text{Re}\mathcal{A}_{\text{reg}}(\tau_0)$ of the TEE as a function of τ_0 (with $\omega = 1.65$, $\ell_{\text{AdS}} = 1$ and $d = 3$) is shown in Fig. 5. The cases of different ω and dimensions $d \geq 3$ are similar to each other.

Notice that for the specific case of $d = 2$ (BTZ black hole), the exponent $2d - 4$ in Eqs. (2.29) and (2.30) vanishes. Taking the metric function as $f(r) = r^2 - M$ (setting $\ell_{\text{AdS}} = 1$ and M to represent the mass parameter), the integral simplifies to a logarithmic form. Explicitly, the regularized integration yields:

$$\begin{aligned} \text{Re}\mathcal{A}|_{d=2} &= \int_0^{1/\epsilon} \frac{dr}{\sqrt{r^2 + (H_*^4 - M)}} \\ &= \ln \left(r + \sqrt{r^2 + H_*^4 - M} \right) \Big|_0^{1/\epsilon} \\ &\approx \ln \frac{2}{\epsilon} - \ln(H_*^4 - M) . \end{aligned} \tag{2.34}$$

This explicitly exhibits the logarithmic UV divergence $\ln(1/\epsilon)$ characteristic of CFT_2 , which is effectively removed by the subtraction scheme Eq. (2.32).

2.3.2 Imaginary part

The imaginary part of the TEE arises physically from the area of the time-like segment A_2B_2 , which connects the past and future singularities. As established in Sec. 2.2, for the minimal configuration, this segment passes through the bifurcation surface H , as shown in Fig. 3(b). To calculate its area, we evaluate the area of a surface at constant t and x ,

extending from the singularity $r = 0$ to the horizon $r = r_h$ (the radius of the horizon r_h has been defined in Eq. (2.3), satisfying $r_h^d = \omega^{d-2} \ell_{\text{AdS}}^2$) and back. The induced metric on this codimension-2 time-like surface is

$$ds_{\text{TL}}^2 = -\frac{dr^2}{f(r)} + r^2 d\mathbf{y}_{d-2}^2 , \quad (2.35)$$

Notice that inside the horizon ($r < r_h$), the function $f(r)$ is negative. Consequently, the area element is $d\text{Im}\mathcal{A} = \sqrt{|h|} d^{d-1}y = r^{d-2}/\sqrt{-f(r)} dr d^{d-2}y$. The total imaginary area density $\text{Im}\mathcal{A}(A_1 A_2 B_2 B_1) \equiv \text{Im}\mathcal{A}/\mathcal{V}_{d-2}$ is twice the integral from the singularity to the horizon:

$$\text{Im}\mathcal{A}(A_1 A_2 B_2 B_1) = 2 \int_0^{r_h} dr \frac{r^{d-2}}{\sqrt{-f(r)}} = \frac{2\ell_{\text{AdS}} r_h^{d-2}}{d} B\left(\frac{3}{2} - \frac{2}{d}, \frac{1}{2}\right) , \quad (2.36)$$

where $B\left(\frac{3}{2} - \frac{2}{d}, \frac{1}{2}\right)$ is the Euler beta function. As a consistency check, for $d = 2$ (the BTZ black hole), this formula correctly reproduces the well-known universal result

$$\text{Im}\mathcal{A}(A_1 B_1 B_2 A_2) = 2 \times \frac{\pi \ell_{\text{AdS}}}{2} = \pi \ell_{\text{AdS}} . \quad (2.37)$$

It is exactly what happens in the BTZ black hole [23].

While the real part of the TEE varies with the boundary time width τ_0 , the imaginary part is independent of τ_0 . However, it crucially depends on the black hole thermodynamics (for example, temperature of the black hole). Using the relation between the horizon radius and the Hawking temperature for planar SAdS black holes (2.1),

$$T_H = \frac{dr_h}{4\pi\ell_{\text{AdS}}^2} , \quad (2.38)$$

one can show that $\text{Im}\mathcal{A}$ scales with the Hawking temperature as

$$\text{Im}\mathcal{A} = 2\ell_{\text{AdS}}^{2d-3} \frac{(4\pi)^{d-2}}{d^{d-1}} B\left(\frac{3}{2} - \frac{2}{d}, \frac{1}{2}\right) \times T_H^{d-2} \propto T_H^{d-2} . \quad (2.39)$$

The scaling behavior derived above ($\text{Im}\mathcal{A} \propto T_H^{d-2}$) suggests that, at least within the framework of the CWES proposal, the imaginary part of TEE encodes fundamental information about the thermal properties of the black hole. Since this contribution depends explicitly on the spacetime geometry (specifically, the temperature) for $d \geq 3$, it distinguishes itself from a generic UV cutoff.

However, the interpretation of this imaginary component remains a subject of active discussion. Recent studies utilizing alternative definitions (e.g., Ref. [26]) have suggested that a constant imaginary contribution might be unphysical and could be absorbed into the definition of the UV cutoff, effectively yielding a real-valued TEE. While our results for $d \geq 3$ (which exhibit dynamic dependence on the geometry) suggest that the imaginary part may possess a richer physical structure than previously thought, it is possible that its interpretation depends on the specific computational scheme or dimension. Whether the imaginary part is a universal physical feature or an artifact of specific holographic proposals remains an open and intriguing question. We do not attempt to settle this debate here, but rather highlight it as a compelling direction for future investigation.

2.4 Asymptotic Analysis for Large Temporal Width

Our numerical results show that for large boundary temporal width $\tau_0 \rightarrow \infty$, the real part of the TEE appears to grow linearly with τ_0 , as shown by the black dashed line in Fig. 5. In this section we will verify this asymptotic behavior analytically and numerically.

As suggested by the numerical data in Fig. 6, the limit $\tau_0 \rightarrow \infty$ corresponds to the conserved quantity H_* approaching its minimum value, $H_{*,\min}$, defined by Eq. (2.14). As $H_* \rightarrow H_{*,\min}$, the integrand in both Eqs. (2.29) and (2.30) becomes dominated by the behavior near this critical radius r_c , where r_c is defined in Eq. (2.14). To analyze this, we perform a Taylor expansion of the term X^2 around $r = r_c$. Defining $\delta \equiv H_*^4 - H_{*,\min}^4 \rightarrow 0^+$ and $u \equiv r - r_c$, we find:

$$X \rightarrow \sqrt{\delta + a^2 u^2}, \quad (2.40)$$

where $a^2 = -G''(r_c)/2 > 0$.

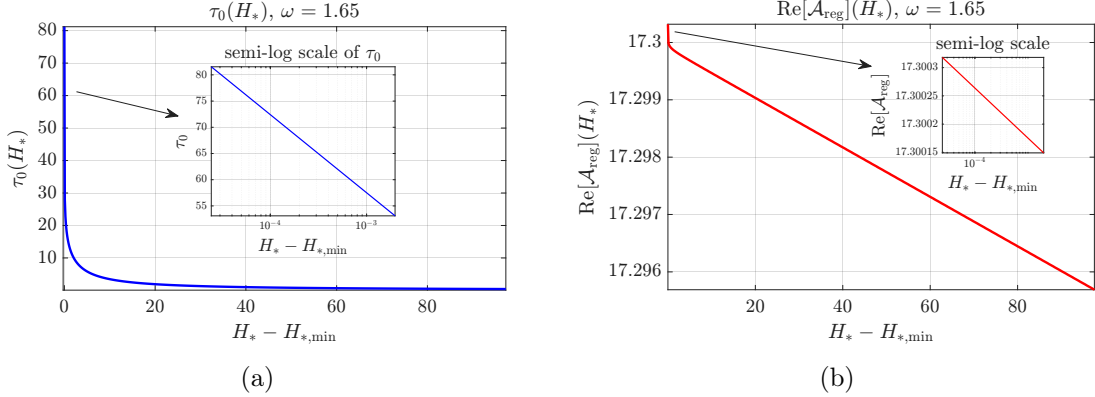


Figure 6: (a) The boundary temporal width $\tau_0(H_*)$ and (b) regularized real area $\text{Re}\mathcal{A}_{\text{reg}}(H_*)$ as functions of the conserved quantity H_* . Both quantities decrease monotonically as H_* increases. The insets show the same data plotted on a semi-logarithmic scale against the distance to the minimum value, $H_* - H_{*,\min}$. The clear linear behavior in these insets provides strong numerical evidence for the logarithmic divergence predicted by Eqs. (2.41) and (2.42).

With this quadratic approximation, our integrals Eqs. (2.29) and (2.30) simplify significantly. When $H_* \rightarrow H_{*,\min}$, $\tau_0(H_*)$ becomes

$$\tau_0(H_*) \approx -\frac{r_c^{2d-4}}{aH_{*,\min}^2} \ln \delta + \text{finite part}. \quad (2.41)$$

Here we have used the fact

$$\int \frac{du}{\sqrt{\delta + a^2 u^2}} = \frac{1}{a} \text{arcsinh} \left(\frac{au}{\sqrt{\delta}} \right),$$

and $\text{arcsinh}(z) \approx \ln(2z)$ for $z \rightarrow \infty$. While for $\text{Re}\mathcal{A}_{A_1 A_2}(H_*)$, as $H_* \rightarrow H_{*,\min}$ we also have

$$\text{Re}\mathcal{A}_{A_1 A_2}(H_*) \approx -\frac{r_c^{2d-4}}{a} \ln \delta + \text{finite part}. \quad (2.42)$$

This analysis predicts that both temporal width $\tau_0(H_*)$ and area $\text{Re}\mathcal{A}(H_*)$ should diverge logarithmically as $H_* \rightarrow H_{*,\min}$ (i.e., as $\delta \rightarrow 0$). This precise logarithmic behavior is explicitly confirmed in our numerical results. As shown in the insets of Fig. 6(a) and 6(b), when plotted on a semi-logarithmic scale against $H_* - H_{*,\min}$, both $\tau_0(H_*)$ and $\text{Re}\mathcal{A}(H_*)$ exhibit a clear linear relationship, which is the signature of a logarithmic divergence.

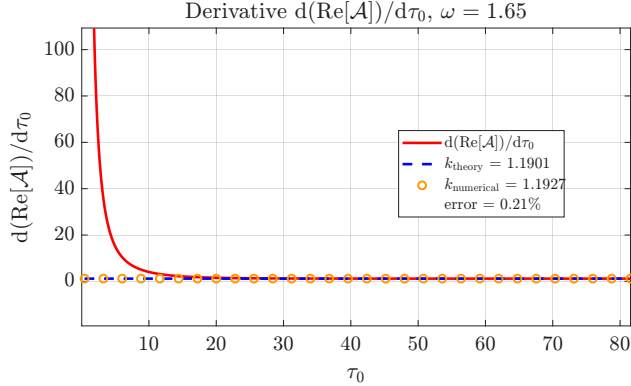


Figure 7: Comparison between the numerical and theoretical growth rates of TEE. The solid red curve denotes the numerical derivative $d(\text{Re}\mathcal{A})/d\tau_0$. The dashed black line represents the theoretical asymptotic slope k_{theory} predicted by Eq. (2.43). The yellow circles highlight the numerical data in the large τ_0 regime, indicating convergence to the theoretical limit.

By eliminating the $\ln \delta$ term between these two asymptotic analysis expressions Eq. (2.41) and Eq. (2.42) for large $\tau_0 \rightarrow \infty$, we obtain a direct linear relationship between them:

$$\text{Re}\mathcal{A}_{A_1 A_2 B_2 B_1}(\tau_0) \approx 2H_{*,\min}^2 \tau_0 + \text{finite part} , \quad \text{as } \tau_0 \rightarrow \infty , \quad (2.43)$$

which means we can theoretically calculate the slope $k_{\text{theory}} = 2H_{*,\min}^2$ of linear growth $\text{Re}\mathcal{A}(\tau_0) = k_{\text{theory}} \cdot \tau_0$ for large $\tau_0 \rightarrow \infty$. This linear relationship implies that the growth rate k_{theory} of TEE should asymptotically approach a constant value. To verify this prediction, we numerically compute the derivative $d(\text{Re}\mathcal{A})/d\tau_0$ and compare it against this theoretical slope. As illustrated in Fig. 7, the numerical derivative converges precisely to the predicted constant in the large $\tau_0 \rightarrow \infty$ limit. This agreement confirms the validity of our asymptotic analysis.

3 Time-like Entanglement in Hairy Black Holes

In the previous section, we established a robust framework for calculating the TEE and applied it to the SAdS black hole. The discussion in Sec. 2 relied on a specific geometric feature: the causal structure of the singularity permits space-like extremal surfaces with non-zero area to connect the boundary to the interior. However, this causal structure is not universal to all black holes. In particular, the geometric properties of simple vacuum solutions like the SAdS and BTZ black holes are not universal. Moving beyond simple

vacuum solutions, one encounters spacetimes where matter backreaction fundamentally alters the interior causal structure.

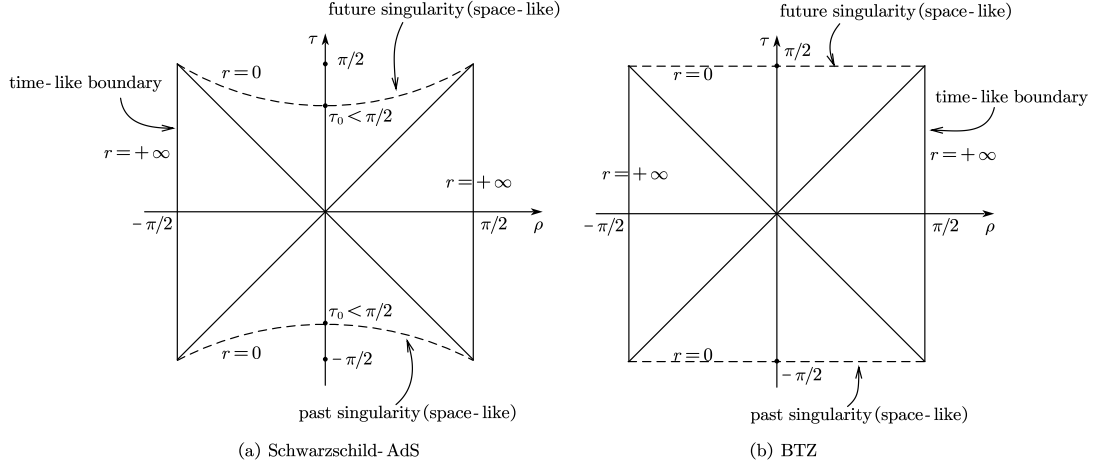


Figure 8: (a) Penrose diagram of AdS-Schwarzschild black hole, where the space-like singularity behaves as ‘concave’. (b) Penrose diagram of the BTZ black hole, where the space-like singularity is represented as a horizontal straight line.

In fact, the interior causal structure of spacetime will constrain the behavior of both space-like and time-like extremal surfaces. This structure is clearly reflected in the geometry or ‘shape’ of the Penrose diagram. For instance, for a SAdS black hole, the space-like singularity is depicted as a ‘concave’ curve, as shown in the Penrose diagram in Fig. 8(a). Specifically, the $d = 2$ BTZ black hole is similar to SAdS case, while with the slight difference that its space-like singularity is drawn as a parallel direction of space-like straight line(as illustrated in Fig. 8(b)), and the overall Penrose diagram shows a square shape. In contrast, for black holes with scalar hair, the singularity can become ‘convex’ [15, 42]. We will demonstrate that this geometric shift forces the TEE of small boundary temporal width to enter a novel ‘time-like phase’, where the time-like entanglement entropy originates solely from the time-like extremal surface, with the space-like contribution reduces to a UV regulator effect. A detailed discussion will be provided in Sec. 3.3.

To investigate this phenomenon, we turn our attention to a well-understood, non-vacuum solution: the hairy black hole that arises in the context of holographic superconductivity. This system serves as an ideal laboratory to classify these interior structures and to study the emergence of this time-like entanglement.

3.1 Classifying Black Hole Interiors

3.1.1 Type-I/II spacetimes

Consider a static black hole possessing a single event horizon with non-zero surface gravity; in such cases, the singularity is typically space-like. We begin by introducing a criterion based on the causal nature of the singularity to classify such spacetimes as either *Type-I* or *Type-II*, and proceed to confirm that the SAdS black hole in Sec. 2 and BTZ black hole belong to the Type-I category.

The idea of classifying black hole interiors based on their causal “shape” is not new. Pioneering work used the behavior of ingoing null geodesics to describe the “shape” of Penrose diagram relative to the boundary [16]. More recently, this classification has been explored in the context of the Complexity=Action (CA) conjecture, where the geometry of the Wheeler-DeWitt patch led to a distinction between “Type-D” (down) and “Type-U” (up) spacetimes [15, 42, 43]. These classifications describe the same underlying physical dichotomy; our Type-I (concave) spacetimes correspond to the Type-D (down) cases, while our Type-II (convex) spacetimes correspond to the Type-U (up) cases. We adopt the Type-I/II nomenclature in this work. These findings suggest that such a classification reflects a robust feature of black hole interior geometry.

To define the these two kinds of spacetimes, we consider the in-falling null sheet that starts from the opposite boundary at coordinate time $t = 0$. Such a null sheet will meet the singularity at coordinate time t_0 . In order to find the value of t_0 , we transform into the Eddington coordinates defined in Eq. (2.10). In-falling light rays follow paths of constant $v = t + r_* = \text{const}$, which are indicated by the red lines in Fig. 9. For the null sheet starting from boundary with $t = 0$, we have $v = t + r_* = 0 + r_*(\infty) = 0$. When the null sheets reach the singularity, the time t_0 is given by the equation

$$t = t_0 \equiv - \int_{\infty}^0 \frac{d\tilde{r}}{f(\tilde{r})} . \quad (3.1)$$

Based on the sign of t_0 , which characterizes the “degree of concavity (or convexity)” of the space-like singularity of spacetime, we classify spacetimes into two families (see Fig. 9):

- **Type-I (Concave/Flat Singularity):** $t_0 \geq 0$, the singularity is “concave” (shown in Fig. 9(a)) or “flat”(shown in Fig. 9(b)). Two null sheets coming from $t_L = t_R = 0$ will first meet the space-like singularity at $r = 0$ before their coordinate time t decreases into negative. Two typical examples are SAdS ($t_0 > 0$) and BTZ ($t_0 = 0$) black holes⁷. In this scenario, the CWES and the behavior of TEE will be similar to what we have found in SAdS case in Sec. 2.
- **Type-II (Convex Singularity):** If $t_0 < 0$, the singularity is “convex”, as shown in Fig. 9(c). The light rays will meet each other before they arrive at the singularity. As we will argue in Sec. 3.2, this seemingly minor change in causal structure has dramatic consequences: for small boundary temporal width, the TEE comes only from a time-like entanglement contribution, with the space-like contribution reduces to a UV regulator effect.

This classification, being rooted purely in the causal structure deep within the horizon, defines two distinct causal phases of the black hole interior, which we label as *Type-I* and *Type-II*.

⁷While other classification schemes (e.g., Ref. [15]) may treat the $t_0 = 0$ case as a distinct critical scenario, our classification is based on the behavior of the Time-like Entanglement Entropy (TEE). From the perspective of TEE, the crucial distinction is simply whether a non-zero “time-like entanglement gap” τ_c is required for its definition, as we will discuss in Sec. 3.3. Since for both $t_0 > 0$ and $t_0 = 0$ this gap is absent ($\tau_c = 0$), we group them together as Type-I.

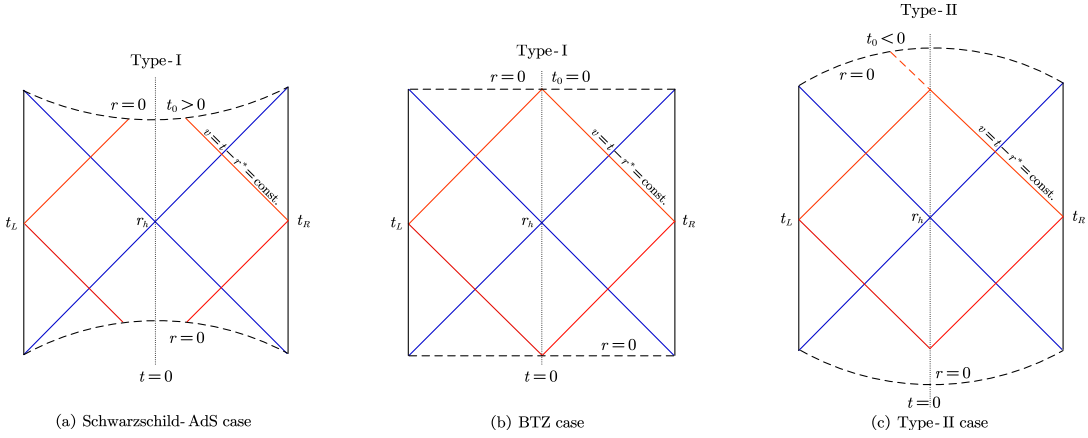


Figure 9: Red lines denote the null sheets that start from boundary and end at the singularities. (a) In SAdS case, the time t_0 is greater than zero, which shows that the space-like singularity behaves as “concave”. (b) In BTZ case, the time t_0 is exactly zero, which shows that the “shape of spacetime” is “square”. They all belong to Type-I spacetime. (c) In Type-II case, the time t_0 is less than zero, which shows that the space-like singularity behaves as “upward convex”.

To apply this criterion, we must evaluate the integral for t_0 . This presents a technical challenge: taking the SAdS black hole as an example, the integrand $1/f(r)$ leads to a logarithmic divergence at the event horizon $r = r_h$, where $f(r_h) = 0$. However, the logarithmic divergence encountered when integrating from the outside ($r > r_h$) to the horizon is precisely canceled by the divergence from the inside ($r < r_h$). To see this, notice that $r = r_h$ is a simple pole of the integral, then we could separate the principal value part at the horizon from the integral, leading to a numerically stable form

$$\int_{+\infty}^r \frac{dr}{f(r)} = \int_{+\infty}^r dr \left(\frac{1}{f(r)} - \frac{2r_h}{f'(r_h)(r^2 - r_h^2)} \right) + f'(r_h)^{-1} \ln \left| \frac{r - r_h}{r + r_h} \right|. \quad (3.2)$$

Notice that when on the boundary $r \rightarrow \infty$ and at the singularity $r \rightarrow 0$, the term $f'(r_h)^{-1} \ln |(r - r_h)/(r + r_h)|$ in Eq. (3.2) actually does not contribute to integral, which means in following calculations we can drop this term. We then obtain

$$t_0 = - \int_{+\infty}^0 dr \left(\frac{1}{f(r)} - \frac{2r_h}{f'(r_h)(r^2 - r_h^2)} \right). \quad (3.3)$$

From this formula one can verify that the SAdS black hole has $t_0 > 0$ and BTZ black hole has $t_0 = 0$, and so both belong to Type-I case.

Having established our criterion and validated it, we now generalize it for general static, planar-symmetric black hole spacetimes that will be the focus of the rest of our investigation. Consider a general metric of the form (z_h is the position of horizon, i.e., $g(z_h) = 0$)

$$ds^2 = \frac{1}{z^2} \left[-g(z)e^{-\chi(z)} dt^2 + g^{-1}(z) dz^2 + dx^2 + d\mathbf{y}_{d-2}^2 \right]. \quad (3.4)$$

Introducing the in-falling null coordinate

$$\begin{aligned} v &= t - z^*(z) , \\ z^*(z) &= \int_0^z dz g^{-1} e^{\chi/2} , \end{aligned} \quad (3.5)$$

the in-falling null sheets are given by the equation

$$v = t - z^*(z) = \text{const.} . \quad (3.6)$$

In this case the same logic applies, and the regularized time t_0 of in-going null sheets from boundary meeting singularity of metric (3.4) is determined by the equation:

$$t_0 = \int_0^\infty dz \left(g^{-1}(z) e^{\chi(z)/2} - \frac{2e^{\chi(z_h)/2} z_h}{g'(z_h)(z^2 - z_h^2)} \right) . \quad (3.7)$$

The sign of this quantity will serve as our guide in exploring novel phenomena in more complex spacetimes, such as hairy black holes.

3.1.2 The Type-II interior from holography

To provide a concrete example of a spacetime where the space-like singularity behaves convexly (i.e., Type-II interior), we now turn to the well-studied $D = (d + 1)$ -dimensional Einstein-Maxwell-scalar model, which provides the standard holographic description of a superconductor [46, 47]

$$I = \frac{1}{16\pi} \int d^D x \sqrt{-g} \left(R + \frac{(D-2)(D-1)}{\ell_{\text{AdS}}^2} - \frac{1}{4} F^2 - |D\Phi|^2 - m^2 |\Phi|^2 \right) , \quad (3.8)$$

where R is the Ricci scalar of spacetime, $F_{\mu\nu} = (dA)_{\mu\nu}$ and $D_\mu = \nabla_\mu - iqA_\mu$. When the temperature is high enough, the solution is a planar Reissner-Nordström-AdS black hole, which possesses a Cauchy horizon and a time-like singularity. When temperature is lower than a critical value T_c , the superconducting phase transition happens, the Cauchy horizon disappears and the singularity will become space-like. With decreasing temperature, the backreaction of matter fields can sufficiently alter the interior geometry to make the singularity “convex” ($t_0 < 0$) [42]. After the superconducting phase transition happens, planar-symmetric hairy black hole and matter fields ansatz can be written in the general form:

$$\begin{aligned} ds^2 &= \frac{1}{z^2} \left(-g(z) e^{-\chi(z)} dt^2 + g^{-1}(z) dz^2 + dx^2 + dy_{d-2}^2 \right) , \\ A_\mu &= A_t(z)(dt)_\mu , \\ \Phi &= \phi(z) . \end{aligned} \quad (3.9)$$

Here the metric functions $g(z)$ and $\chi(z)$ now encode the effects of both the black hole’s mass and charge, and the profile of the scalar hair. In this coordinate system, the spacetime boundary is located at $z = 0$ and the singularity of black hole lies at $z \rightarrow \infty$. With this ansatz, the Hawking temperature T could be expressed as

$$T = -\frac{e^{-\chi(z_h)/2} g'(z_h)}{4\pi} . \quad (3.10)$$

The solutions of these functions can be obtained numerically [46, 47].

For each numerically-obtained matter field and hairy black hole metric field solution (3.9) (parameterized by its temperature T), we can compute the time t_0 that null sheets reach the singularity from the boundary using our generalized formula in Eq. (3.7). The result of this procedure for a standard holographic superconductor model (with $m^2 = -2, q = 1$ in $d = 3$) is presented in Fig. 10. The plot of t_0 as a function of the normalized temperature T/T_c shows precisely the behavior we anticipated. At very low temperatures, t_0 is positive (indicating Type-I interior). However, as the temperature increases towards the critical temperature T_c of the superconductor phase transition, t_0 decreases, crosses zero, and becomes negative. This unambiguously demonstrates that Type-II spacetimes are physically realizable within this well-understood framework.

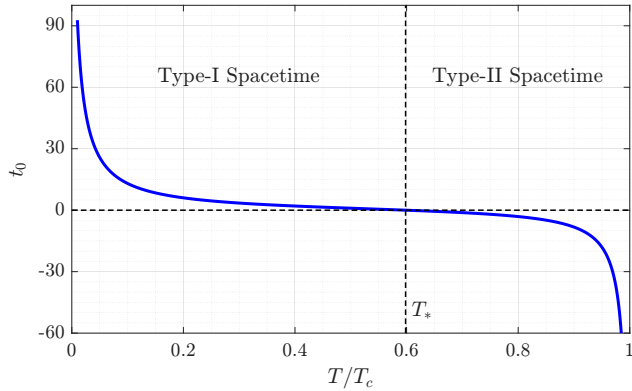


Figure 10: When $d = 3, m^2 = -2, q = 1$, the result of t_0 as the function of T/T_c shows that when approaching the critical temperatures, t_0 becomes negative, the spacetime belongs to the Type-II class. T_* denotes the critical temperature for the phase transition from Type-II to Type-I spacetime.

It is important to note that the holographic superconductor model itself is not crucial in this context; it serves merely as an example that generates a Type-II interior and provides numerical results for the Type-I/II classification criteria. The phenomenon is general: Type-II behavior typically arises from specific deformations of an unstable inner Cauchy horizon, a sufficiently small perturbation can destroy the inner horizon and produce a Type-II interior [5, 42].

3.2 Time-like Entanglement Phase in Type-II Spacetimes

In the previous section, we found that hairy black holes can exhibit a Type-II interior, characterized by a “convex” singularity with $t_0 < 0$. This seemingly minor causal geometric change has a dramatic consequence for TEE: for Type-II interiors, there exists a distinct “time-like entangled phase” for narrow boundary strips. In this phase, the space-like contribution to the TEE reduces to a UV regulator effect, and the TEE is determined solely by the area of time-like extremal surfaces.

We now present the proof for this conclusion. Let us first consider a CWES anchored on a boundary strip of temporal width τ_0 . An ingoing null ray from the boundary point $A_1(t = \tau_0/2)$ reaches the singularity at a coordinate time $t|_{r=0} = \tau_0/2 + t_0$. This null sheet gives the boundary of the future “light cone” of A_1 . Due to causality, any space-like segment A_1A_2 anchored at A_1 must remain outside of this light cone, i.e., the “endpoint” A_2 should satisfy $t|_{A_2} < \tau_0/2 + t_0$. Similarly, any space-like segment B_1B_2 anchored at B_1 must remain exterior of the past light cone of B_1 and the “endpoint” B_2 should satisfy $t|_{B_2} > -(\tau_0/2 + t_0)$. If we choose a sufficiently small temporal width $\tau_0 < -2t_0$ (recalling that $t_0 < 0$ in Type-II spacetime), we find that $t|_{A_2} < 0$ and $t|_{B_2} > 0$ for any valid space-like extremal surfaces A_1A_2 and B_1B_2 . This implies that the entire causally accessible region for both segments, A_1A_2 and B_1B_2 , lies strictly to the left of the vertical $t = 0$, as illustrated in Fig 11(a). As a result, it is geometrically impossible to construct a time-like extremal surface connecting A_2 and B_2 that passes through the bifurcation surface H in Type-II spacetime for narrow boundary strips.

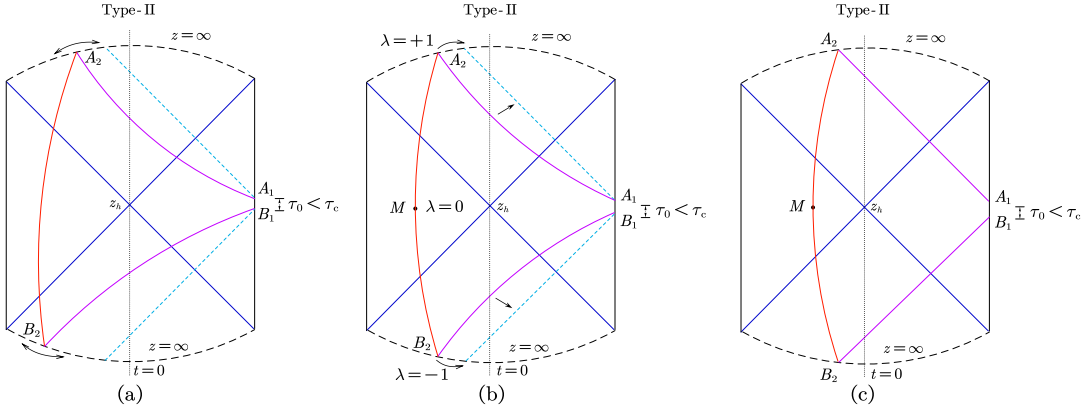


Figure 11: CWES configurations in the “time-like phase” for $\tau_0 < -2t_0$. Blue dashed lines indicate ingoing null sheets from boundary endpoints A_1 and B_1 . Due to causality, space-like segments (purple lines) are confined to the left of these null sheets, as seen in (a) and (b). For non-symmetric configuration (a), one can move the “endpoints” A_2 and B_2 towards opposite directions without changing the area of time-like part and so obtain the configuration (b). The minimal area is achieved in the limiting configuration (c), where these space-like segments will become null surfaces with zero area, leaving only the time-like segment (red line) to contribute to the TEE. It should be noted that, though most parts of A_1A_2 and B_1B_2 are along two 45° lines, their intersections with AdS boundary are still “perpendicular” (this is not exhibited in this figure, see Fig. 18). In fact, the limit where a space-like extremal surface approaches a null hypersurface involves a more subtle regulator effect, which needs to impose both spatial and temporal UV cut-offs. We will discuss this in Sec. 3.3.

In order to explain what this restriction will bring to the TEE, we start from the general setup in Fig. 11(a). By the requirement of extreme condition of TEE, we should begin

by taking the time-like surface to be extreme. Suppose the time-like extremal surface has endpoints A_2, B_2 that lie asymmetrically on the upper and lower singularities. One can move these two endpoints along opposite directions without changing the total time-like area until the surface becomes the symmetric configuration with $t|_{A_2} = -t|_{B_2}$, and still remain to the left of the vertical dashed line $t = 0$, shown in Fig. 11(b). Therefore, without loss of generality, we can restrict our search for the minimal CWES to symmetric configurations where $t|_{A_2} = -t|_{B_2}$. The symmetric codimension-2 time-like extremal surface A_2, B_2 can be parameterized by $\{t = t(\lambda), z = z(\lambda), x = 0, \mathbf{y}_{d-2} \in \mathbb{R}^{d-2}\}$. For the symmetric configuration, we choose the middle point M at $\lambda = 0$ with $t(\lambda = 0) = t_M = 0$ and $z(\lambda = 0) = z_M$. The endpoints A_2, B_2 are set by $A_2 : \lambda = +1$ and $B_2 : \lambda = -1$ at the upper and lower singularities respectively.

The induced metric and the time-like area density functional \mathcal{S}_{TL} for this time-like surface are

$$\begin{aligned} ds^2 &= \frac{1}{z^2} \left[-g(z)e^{-\chi(z)} \dot{t}^2 d\lambda^2 + g^{-1}(z) \dot{z}^2 d\lambda^2 + d\mathbf{y}_{d-2}^2 \right], \\ \mathcal{S}_{\text{TL}} &\equiv \text{Im}\mathcal{A} = 2 \int_{\lambda=0}^{\lambda=+1} d\lambda L, \end{aligned} \quad (3.11)$$

where $L = z^{1-d} \sqrt{g(z)e^{-\chi(z)} \dot{t}^2 - g^{-1}(z) \dot{z}^2}$ is the Lagrangian functional. Notice that L does not depend explicitly on generalized coordinate t , hence there is a conserved momentum Π

$$\Pi = \frac{\partial L}{\partial \dot{t}} = \frac{t z^{1-d} g(z) e^{-\chi(z)}}{\sqrt{g(z)e^{-\chi(z)} \dot{t}^2 - g^{-1}(z) \dot{z}^2}}. \quad (3.12)$$

At the symmetric midpoint M , we have $z(\lambda = 0) = z_M, \dot{z}(\lambda = 0) = 0$. Note that $\dot{t} < 0$ around M since the time-like Killing vector ∂_t points down around M , which is opposite to the direction of increasing affine parameter λ . Substituting this $\dot{t}|_M < 0$ and $\dot{z}|_M = 0$ back into the expression for the conserved momentum Π , we will get

$$\Pi(z_M) = -\frac{\sqrt{g(z_M)e^{-\chi(z_M)}}}{z_M^{d-1}} < 0. \quad (3.13)$$

Since $z_M > 0$ and $g(z_M) > 0$ outside the horizon, the conserved momentum Π is strictly negative.

According to Hamilton-Jacobi theory, the variation of the on-shell time-like area \mathcal{S}_{TL} with respect to its time t_{A_2} of upper endpoint is given by this conserved momentum

$$\frac{\partial \mathcal{S}_{\text{TL}}}{\partial t_{A_2}} = 2\Pi|_{A_2} < 0. \quad (3.14)$$

The factor of 2 arises because the constraint requirement $t|_{B_2} = -t|_{A_2}$ implies that the lower endpoint B_2 varies simultaneously. Since Π is constant along the time-like surface and $\Pi|_M < 0$, we have rigorously proven that $\frac{\partial \mathcal{S}_{\text{TL}}}{\partial t_{A_2}} < 0$.

Eq. (3.14) provides the critical insight: the derivative is strictly negative, which implies that the time-like area \mathcal{S}_{TL} monotonically decreases as the endpoint A_2 and B_2 move to the right (increasing t_{A_2} , but decreasing t_{B_2}). Consequently, the infimum of the time-like area

is achieved at the maximum value of t_{A_2} allowed by causality. In other words, among all candidate extremal surfaces, the time-like extremal surface reaches its infimum in the limit where the configuration from Fig. 11(b) approaches the configuration shown in Fig. 11(c). In that limit, the space-like extremal surfaces approach the null configurations anchored at A_1 and B_1 (purple lines in Fig. 11(c)). Since both components simultaneously approach their respective infimum at this limiting configuration, the global minimum of the total area is realized precisely in this “null limit” (Fig. 11(c)).

It is important to emphasize that this null limit is the “limit” of a family of space-like surfaces which are all “perpendicular to” the AdS boundary. As a result, though the surfaces will increasingly resemble null surfaces in the region far away from the AdS boundary, their UV behaviors always keep “perpendicular to” boundary rather than intersect with the AdS boundary at a 45° angle. In this null limit, the contribution from space-like terms yields a non-zero value due to this UV regularization effect, in contrast to the strict zero expected from a purely null surface. We will analyze this null limit in Sec. 3.3 and show that it is governed by a connection between the UV cutoff on the AdS boundary and the cutoff regulating the approach to the null surface. Up to this regulator effect, the imaginary part from the time-like surface dominates the behavior of the TEE. Therefore, in this regulated sense, we can identify the existence of a “time-like entanglement phase” for small temporal width in Type-II interior.

3.3 Phase Transition of Time-like Entanglement

As we increase boundary temporal width τ_0 , the endpoint $t_{A_2} = t_0 + \tau_0/2$ is pushed towards the future. For Type-II geometries we have $t_0 < 0$, this defines a critical threshold τ_c

$$\tau_c \equiv -2t_0, \quad (3.15)$$

where t_0 is defined in Eq. (3.7). If $\tau_0 < \tau_c$, both endpoints A_2, B_2 lie on the same side of the vertical dashed line $t = 0$, as shown in Fig. 12(a). In this regime the TEE is contributed only by the time-like extremal surface up to a regulator effect, as we have discussed in Sec. 3.2. In this case, the imaginary part of TEE decreases with increasing temporal width of boundary strip, and though the extremal surfaces $A_1 A_2$ and $B_1 B_2$ are “most” null, the UV cut-off effect may yield a non-zero real part. When $\tau_0 = \tau_c$, the two endpoints A_2 and B_2 now lie on a critical line, the TEE is given by a critical configuration as illustrated in Fig. 12(b). When $\tau_0 > \tau_c$, A_2 and B_2 could lie on opposite sides of $t = 0$ and time-like extremal surface can pass through the bifurcation of event horizon (see Fig. 12(c)). In this case TEE acquires both time-like and space-like contributions and the situation reduces to the Type-I case, which have been analyzed in Sec. 2. In this regime, the imaginary part of TEE becomes saturated and keeps constant, but the real part of TEE begins to increase with the temporal width τ_c .

Thus, for $\tau_0 \in [0, \tau_c]$ the TEE probe measures only time-like entanglement. At $\tau_0 \geq \tau_c$, the time-like contribution becomes “saturated” and the space-like contribution appears. The window of boundary time $[0, \tau_c]$ therefore defines a time-like entanglement range, or “time-like entanglement gap”, and the emergence of this gap is the central signature of a

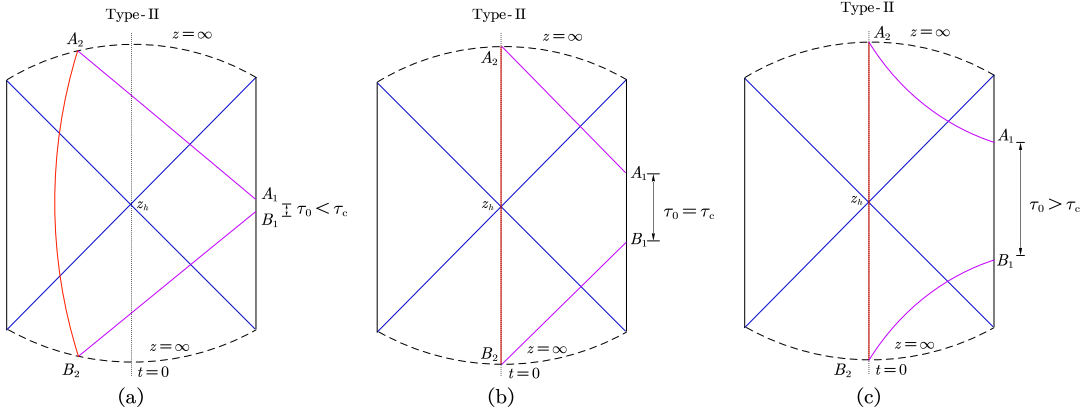


Figure 12: There are three possible CWESs configurations in the Type-II spacetime. (a) When $\tau_0 < \tau_c$, only time-like entanglement contributes to time-like entanglement entropy, up to a regulator effect. (b) TEE is given by a critical configuration, where time-like contribution becomes “saturated”. (c) In $\tau_0 > \tau_c$, TEE reduces to the case of Type-I spacetime, which have been discussed in Sec. 2. Once again, though most parts of A_1A_2 and B_1B_2 in (a) and (c) are along two 45° lines, their intersections with AdS boundary are still “perpendicular” (this is not exhibited in these figures, see Fig. 18).

Type-II interior. For a general metric of the form (3.4), we could express the gap τ_c as follows

$$\tau_c = -2t_0 = -2 \int_0^\infty dz \left(g^{-1}(z) e^{\chi(z)/2} - \frac{2e^{\chi(z_h)/2} z_h}{g'(z_h)(z^2 - z_h^2)} \right). \quad (3.16)$$

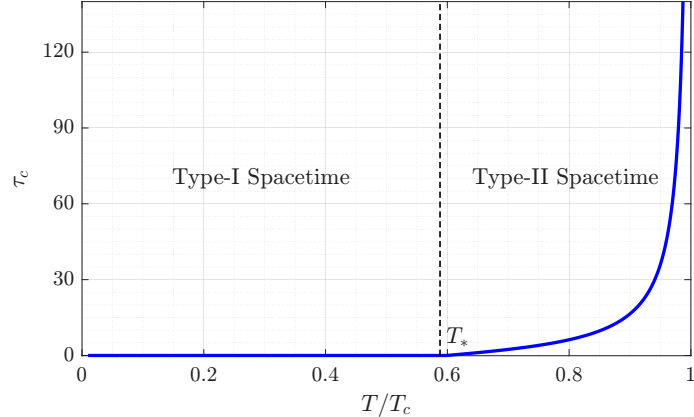


Figure 13: Order parameter τ_c as the function of temperature T/T_c . T_* is the critical temperature for the phase transition from Type-II to Type-I spacetime.

As an example, we study the behavior of TEE in Type-II spacetime based on holographic hairy black hole solutions (3.8). In this model, we could numerically express the time-like entanglement gap τ_c (3.16) as the function of temperature T/T_c , shown in Fig. 13.

This reveals a causal phase transition, entirely distinct from the well-known superconducting phase transition, governed by the causal structure of the black hole interior, where the behavior of time-like entanglement entropy is completely different in Type-I and Type-II spacetimes.

Therefore, critical temporal width τ_c acts as an “order parameter” for this transition. As shown in Fig. 13, it cleanly distinguishes the two phases: it is identically zero in the Type-I phase ($T < T_*$) and becomes non-zero in the Type-II phase ($T > T_*$), the phase transition occurs at the critical temperature (as marked by the vertical dotted line in Fig. 13), T_* , where the order parameter vanishes $\tau_c(T_*) = 0$. Notice that it is important not to confuse this T_* with condensation critical temperature T_c of the holographic superconductor discussed earlier. The size of order parameter, τ_c , grows as the temperature increases above T_* , as quantified in the phase diagram (Fig. 13) and analyzed asymptotically in Fig. 14. Fig. 14(a) shows that, as $T/T_c \rightarrow 1^-$, τ_c exhibits a reciprocal-type divergence, roughly $\tau_c \sim (1 - T/T_c)^{-1}$. Fig. 14(b) shows that near T_* (zero point of order parameter $\tau_c(T_*) = 0$), the behavior of τ_c follows a linear scaling $\tau_c \sim (T - T_*)/T_c$.

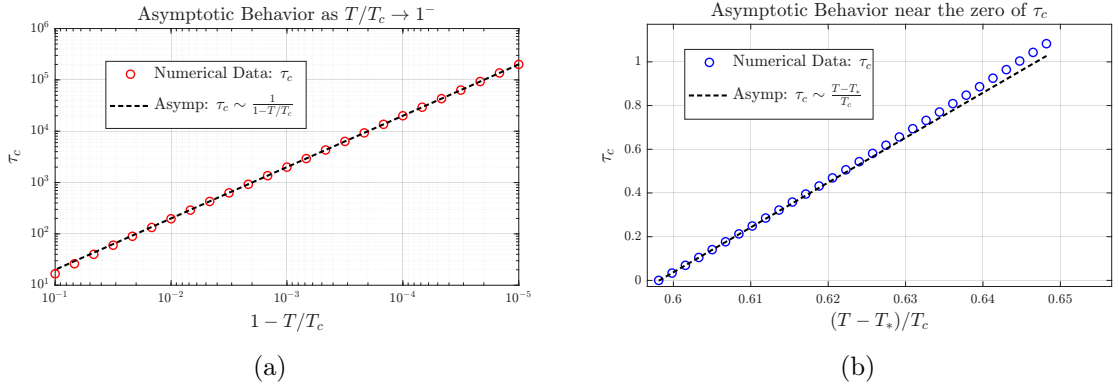


Figure 14: (a) When $T/T_c \rightarrow 1$, the critical length τ_c is approximating a reciprocal-type divergence $\tau_c \sim (1 - T/T_c)^{-1}$. (b) Near T_* , the behavior of τ_c follows a linear scaling, which behaves as $\tau_c \sim (T - T_*)/T_c$.

The phase diagram Fig. 13 reveals a rich structure. At high temperatures⁸ $T_* < T < T_c$, the system is in the Type-II phase ($\tau_c \neq 0$). As we decrease the temperature, the system undergoes a phase transition at $T_* \approx 0.58T_c$, entering the Type-I phase. Deeper in the Type-II phase, as T approaches the superconducting critical temperature T_c , the required minimum temporal width τ_c grows without bound. This signals a dramatic change in the interior geometry and causes the boundary’s time-like entanglement range to expand rapidly.

This phase transition at T_* leaves sharp, observable signatures in the behavior of the time-like entanglement itself. By applying the numerical framework for computing the

⁸In this paper, we only focus on the situation of $T < T_c$, where the singularity becomes space-like and no inner horizon will appear. For the case $T > T_c$, the interior has Cauchy horizon and the singularity becomes time-like, which leads to additional difficulty in finding the correct configuration of TEE. We leave this subtle issue in future.

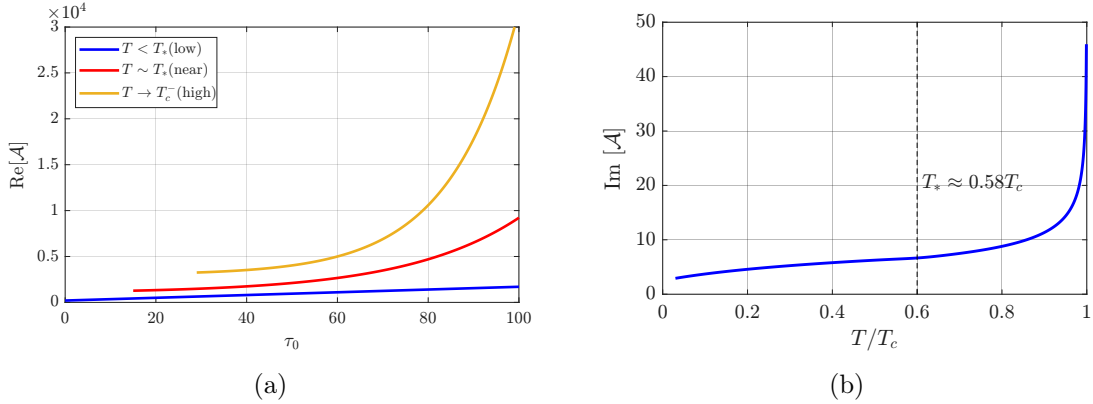


Figure 15: (a) Relationship between $\text{Re}\mathcal{A}$ and τ_0 for different temperatures. In the low temperature $T < T_*$ regime, boundary temporal width τ_0 can start from zero. For temperatures slightly above $T \gtrsim T_*$, a nonzero critical temporal width appears. For the case that temperature is close to critical temperature $T \rightarrow T_c^-$, the real part of TEE grows rapidly and reaches much larger values. (b) When $\tau_0 > \tau_c$, the imaginary part of TEE as the function of temperature T/T_c .

TEE's real and imaginary parts, which we established and validated in Sec. 2, we can now probe these signatures directly. The most direct signature is seen in the real part of the TEE $\text{Re}\mathcal{A}(\tau_0)$, shown in Fig. 15(a):

- For $T > T_*$ (in the Type-II phase, red curve for $T \gtrsim T_*$ and orange curve for $T \rightarrow T_c^-$), a clear “time-like entanglement gap” τ appears, which means the spacetime is in the “gapped” Type-II phase. The real part of TEE, $\text{Re}\mathcal{A}(\tau_0)$, can only begin at the non-zero critical value $\tau_0 = \tau_c$. This entanglement gap is a signature of the Type-II interior. For any boundary width $\tau_0 < \tau_c$, the TEE is only given by the imaginary part of extremal surfaces, leading to a “time-like entanglement” phase.
- For $T < T_*$ (in the Type-I phase, blue curve for $T < T_*$), because the critical separation is zero $\tau_c = 0$, the TEE curve could start from the origin, exhibiting a “gapless” behavior similar to the SAdS case. There TEE contains both time-like entanglement and space-like entanglement contributions, i.e., space-like entanglement re-emerges. The imaginary part contributes a constant value independent of τ_0 in this phase, because time-like contribution have “saturated”.

Besides the real part of TEE and “entanglement gap” τ_c , the imaginary part $\text{Im}\mathcal{A}$ also serves as a probe of the causal transition from Type-I phase to Type-II phase, exhibiting distinct functional dependencies on temperature T/T_c in the different phases, as shown in Fig. 15(b). The imaginary part of the TEE will monotonically decrease with the decreasing temperature after the superconducting phase transition happens. In addition, we sketch its asymptotic behavior in two limits: the low temperature limit and the approach to the condensation onset (the condensation critical temperature). As illustrated in Fig. 16(a), when low temperature limit $T/T_c \rightarrow 0$, the imaginary part of the TEE shows logarithmic growth, while for the high temperature limit $T/T_c \rightarrow 1$, the imaginary part of the TEE shows a power-law decay.

mic asymptotics $\text{Im}\mathcal{A} \sim \ln(1 - T/T_c)$ (see Fig. 16(a)). As the system approaches the condensation critical temperature $T/T_c \rightarrow 1^-$, in other words $1 - T/T_c \rightarrow 0^+$ (shown in Fig. 16(b)), the imaginary part of the TEE exhibits a clear power-law asymptotics, scaling as $\text{Im}\mathcal{A} \sim (1 - T/T_c)^{-0.21}$.

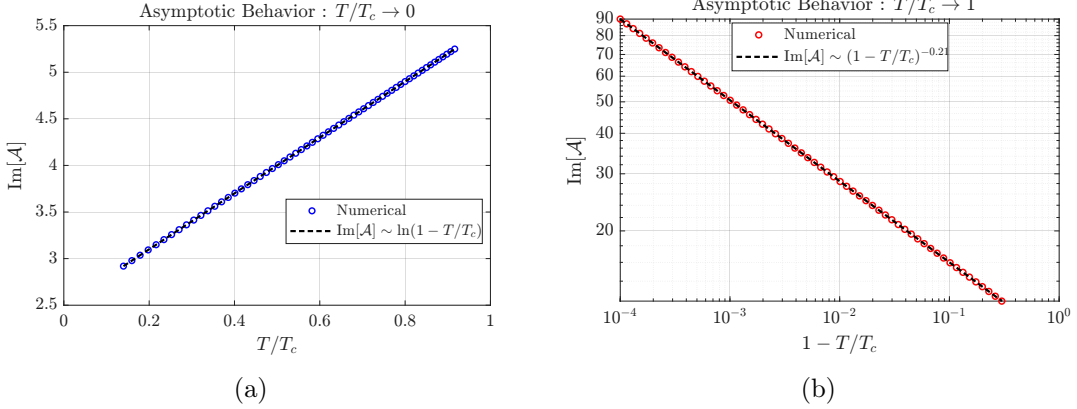


Figure 16: (a) When $T/T_c \rightarrow 0$, imaginary part of TEE $\text{Im}\mathcal{A}$ exhibits a logarithmic divergence $\text{Im}\mathcal{A} \sim \ln(1 - T/T_c)$. (b) When $T/T_c \rightarrow 1^-$, the behavior of $\text{Im}\mathcal{A}$ follows a power-law scaling $\text{Im}\mathcal{A} \sim (1 - T/T_c)^{-0.21}$.

Note that the real part in Type-II spacetime for $\tau_0 < \tau_c$ is obtained via a null-limiting procedure (see Fig. 11). In this null limit, we use a family of space-like surfaces which are all “perpendicular to” the AdS boundary to approach a null surface. As a result, these surfaces will increasingly resemble null in the region far away from the boundary but their UV behaviors always keep “perpendicular to” boundary rather than intersect with the boundary at a 45° angle required by an exact null surface. In that limit the surfaces A_2A_2 and B_1B_2 will become null far away from the AdS boundary, yet the area still produces a non-zero, and in fact unbounded, contribution due to the space-like contribution near AdS boundary. This behavior is controlled by two cutoffs. One is the UV “spatial” cutoff near the AdS boundary. The other is an UV “temporal” cutoff in the time difference $\tau_0 - v_{A_2}$ between the arrival time on boundary of the space-like extremal surface and the corresponding null value of null surface on boundary; this second cutoff measures how closely the space-like surfaces approach the null surfaces. Under the null limit only the divergent spatial and temporal pieces of the space-like extremal surface survive for $\tau < \tau_c$.

To make the role of these cutoffs explicit, note that the null limit corresponds to taking the conserved quantity H_* to infinity value $H_* \rightarrow \infty$. It is convenient to introduce the auxiliary variable $h^{2d-2} \equiv H_*^4$, and for $d = 3$ we have $h = H_*$. The gap between the arrival time on boundary of the space-like extremal surface and the corresponding null value of null surface Δt on boundary actually is $\Delta t = \tau_0/2 - v_{A_2}$. In the large- H_* (large- h) limit, time-gap or time-difference Δt is driven to its asymptotic form Δt_{UV} . One finds (see Appendix B for the derivation)

$$\Delta t_{\text{UV}} = \tau_0(h \rightarrow \infty)/2 - v_{A_2} = \eta_d h^{-1} + \dots, \quad (3.17)$$

where the constants $\eta_d = \frac{1}{\sqrt{\pi}} \Gamma\left(\frac{d}{2d-2}\right) \Gamma\left(\frac{2d-3}{2d-2}\right)$ are defined in Eq. (B.4), and the omitted

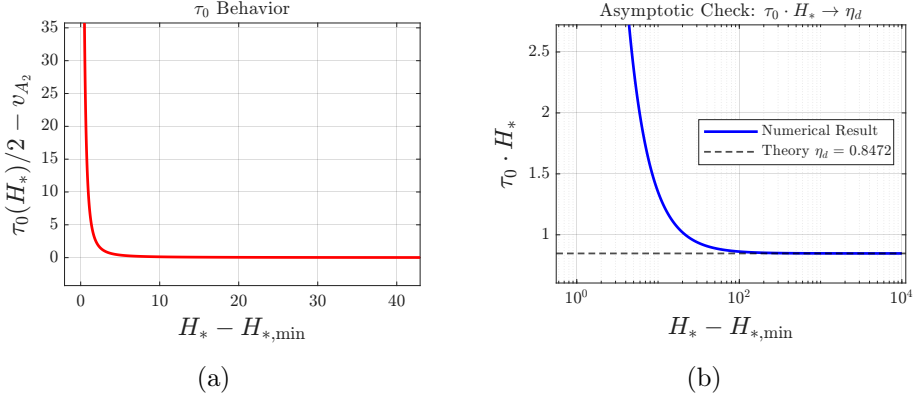


Figure 17: (a) The null limit corresponds to $H_* \rightarrow \infty$ (or $h \rightarrow \infty$), (b) giving $\tau_0/2 - v_{A_2} \sim \eta_d h^{-1}$ and driving the space-like arrival time to the null value (here we have set $d = 3$ and worked in Type-II spacetime for $\tau_0 < \tau_c$). Here η_d is a dimension-dependent constant defined in Appendix B.

terms represent the higher-order terms in h^{-1} that we have neglected. As $h \rightarrow \infty$, the right-hand side behaves as $\Delta t_{\text{UV}} = \tau_0(h)/2 - v_{A_2} \propto h^{-1}$. Numerically, this h^{-1} power-scaling is shown in Fig. 17. Hence the null limit is physically realized by taking the conserved quantity H_* to infinity value, or $h \rightarrow \infty$.

In the null limit the area integral for surface $A_1 A_2$ has the following large- H_* asymptotics (see Appendix B for details and for the definition of β_d)⁹:

$$\mathcal{A}_{A_1 A_2}(H_*) = \frac{\beta_d}{2h^2 z_h^d} + \frac{\epsilon^{2-d}}{d-2} - \eta_d^{d-1} \frac{\Delta t_{\text{UV}}^{2-d}}{d-2} + \dots \quad (3.18)$$

Particularly, we find that there are two kinds of divergencies ϵ and Δt_{UV} in Eq. (3.18). Here ϵ is the UV ‘‘spatial’’ cutoff near the AdS boundary, and Δt_{UV} corresponds to null limit where the space-like extremal surface approaches to null (i.e., $h \rightarrow \infty$). The term ϵ^{2-d} in Eq. (3.18) is the familiar UV contribution from the boundary region. The new term, proportional to $(\Delta t_{\text{UV}})^{2-d}$ (or equivalently h^{d-2}), represents a UV temporal divergence in the null limit. These UV terms ϵ and Δt_{UV} yield a nonzero contribution even when the space-like piece becomes almost null.

The reason is, near the AdS boundary the space-like extremal surface remains nearly orthogonal to the boundary, whereas a true null surface meets the boundary at a 45° angle. The nearly vertical piece therefore always produces a UV contribution to the area that does not vanish in the null limit, as depicted in Fig. 18. As we have known, the spatial UV cut-off ϵ can be interpreted as a the minimal resolution in spatial scale. We can make a similar interpretation for the cut-off Δt_{UV} . From the large- H_* (or large- h) analysis in Eq. (3.17), we see the finite cut-off for Δt_{UV} means we set a minimal value for $\tau/2 - v_{A_2}$. Thus, this is equivalent to set a finite UV ‘‘temporal’’ resolution, as shown in Fig. 18. On

⁹Here we assume $d \geq 3$. In the case $d = 2$, a logarithmic divergency on h will appear. See Eq. (B.9) in Appendix B for details.

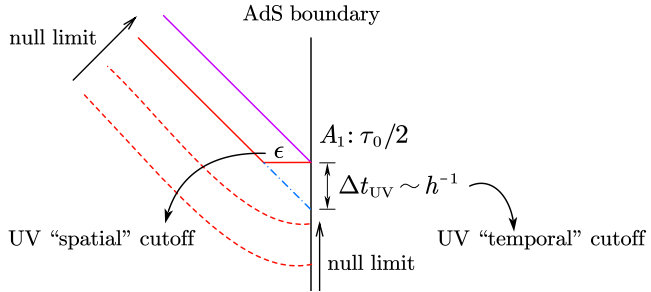


Figure 18: Schematic near-boundary geometry. Red dashed lines show a family of space-like extremal surfaces approaching the null surface (purple solid line). The UV spatial cutoff ϵ imposes a finite spatial “resolution” near the boundary; for spatial scales below ϵ the red and purple curves cannot be distinguished. As the spacelike extremal surface approaches a null configuration, we find that alongside the standard UV spatial cutoff, an additional regulator necessarily emerges. This new cutoff $\Delta t_{UV} \sim h^{-1}$ quantifies the degree of approach to the null limit or, equivalently, how closely the boundary value of the space-like surfaces (blue dashed line) approximate that of the null surface boundary. Cutoff Δt_{UV} sets a UV “temporal” resolution: time differences smaller than $\mathcal{O}(\eta_d h^{-1})$ cannot be resolved.

time scales smaller than this UV cutoff Δt_{UV} one cannot resolve the difference between the arrival time of the space-like extremal surface (red solid curve) and that of the null surface (purple solid curve). Thus both cutoffs, the UV “spatial” cutoff ϵ near the boundary and the UV “temporal” cutoff Δt_{UV} controlled by h , produce residual, non-vanishing contributions to $\text{Re}\mathcal{A}$ in the Type-II spacetimes with $\tau_0 < \tau_c$.

The double limit $T \rightarrow T_c^-$ and $\tau_c \rightarrow \infty$ show that the system exhibits the extreme limit of the Type-II phase. The divergence of τ_c , shown in our phase diagram (Fig. 13), together with the rapid growth of the real part of TEE (orange line in Fig. 15(a)), results from the fact that the space-like extremal surfaces A_1A_2 and B_1B_2 approach the null singularity when $T \rightarrow T_c^-$ and $\tau_0 \rightarrow \infty$.

Physically, this reflects a drastic change of the interior geometry: as the temperature increases to T_c , the space-like singularity disappears, the Cauchy horizon and time-like singularity will recover. We can illustrate this process with a schematic diagram. Fig. 19(a) shows the original space-like singularity of a hairy black hole. As the temperature increases, the time t_0 (3.7) that fall from the boundary to the singularity shifts from positive to negative, causing the space-like singularity to “bulge” as seen in Fig. 19(b). At the critical condensation temperature $T \rightarrow T_c^-$, as the condensation becomes infinitesimally small, the spacetime singularity converges to the null singularity shown in Fig. 19(c). At this point the boundary’s time-like entanglement window grows unbounded (see Fig. 13): for any finite boundary time spacing τ_0 , the TEE is dominated by the time-like contribution (up to the aforementioned regulator effect) because the entanglement gap becomes effectively infinite. The space-like singularity and the Cauchy horizon merge into a null singularity. This again

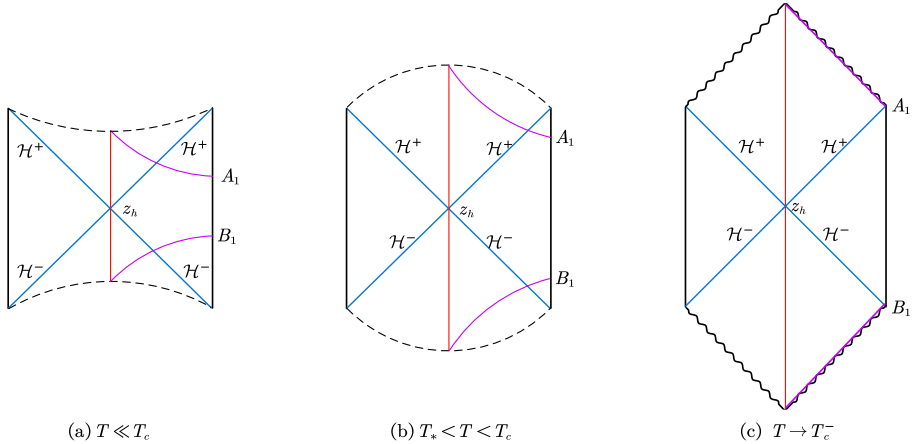


Figure 19: As the temperature increases to the critical condensation temperature $T/T_c \rightarrow 1$, the space-like singularity converges to the null singularity, with the interior geometry transforming from Type-I to Type-II.

highlights the pathological nature of the Cauchy horizon and null singularities, as discussed in the context of the cosmic censorship hypothesis. We therefore conjecture: the presence of an inner Cauchy horizon is associated with a nonzero entanglement gap τ_c in the boundary theory. Further, an infinitesimal perturbation that turns the Cauchy horizon into a null singularity drives $\tau_c \rightarrow \infty$, so that TEE is entering a “pure time-like entanglement phase”, up to a regulator effect.

The nature of the zero-temperature ground state is, however, of key theoretical importance. It is crucial to note that the infrared (IR) geometry of this ground state in holographic superconductors is not universal and depends sensitively on the model parameters m^2 and q , see Ref. [48]. Here we present results for the holographic superconductor model with parameters $m^2 = -2, q = 1$. A full analysis of how the TEE behaves in the qualitatively different ground states that arise in other parameter regimes, such as those with emergent conformal (AdS), Lifshitz geometry or Poincaré symmetry discussed in Ref. [48], is beyond the scope of our current analysis, but presents an intriguing question.

In conclusion, there is causal phase transition between the type II and Type I space-times after the superconducting phase transition happens. Our analysis in this section has uncovered the causal phase transition at a critical temperature T_* within the black hole interior, diagnosed entirely by the time-like entanglement entropy. The properties of TEE on the boundary serve as a remarkably sharp probe of this hidden interior geometry. The properties of TEE on the boundary, therefore, act as a remarkably sharp, single-boundary probe, directly linking a quantum informational quantity to a fundamental change in the bulk’s hidden causal structure.

4 Discussion

Understanding the internal structure of black holes remains a central challenge in holography and gravitational physics. In this work, we approached this problem from a new single-boundary perspective — Time-like Entanglement Entropy (TEE) — and established a consistent and transparent framework for computing it. We first applied this framework to the Schwarzschild-AdS geometry as a controlled baseline. Our analysis demonstrated that the TEE exhibits linear growth in the limit of large temporal width $\tau_0 \rightarrow \infty$, governed by a critical extremal surface. Furthermore, we argued that the imaginary part of the TEE is not merely a regularization artifact; instead, it encodes physical information about the thermal state that cannot be absorbed into a standard UV cutoff. Building on this framework, we uncovered a previously hidden causal phase transition inside the black hole, which is invisible to traditional holographic probes. We identified two distinct interior phases, Type-I and Type-II, distinguished by the causal structure of their space-like singularities. The transition is marked by a new order parameter, the critical temporal width τ_c . This quantity manifests on the boundary as a “time-like entanglement gap”. Inside this gap ($\tau_0 < \tau_c$), TEE is dominated by a “time-like entanglement phase” in Type-II interior, up to a regulator effect corresponding to finite “spatial” and “temporal” resolutions. Crucially, this framework provides a sharp diagnostic for the stability of the black hole interior. We found that the presence of an inner Cauchy horizon drives the critical width τ_c to infinity, resulting in pure time-like entanglement. Unlike “strong probes” that require information from both boundaries to access the singularity, TEE is a single-boundary observable. It therefore enriches the holographic dictionary by directly relating a boundary information measure to the deep dynamical features of the bulk spacetime.

This work lays the foundation for several critical future directions. First, our classification in Sec. 3 relies on space-like singularities. Extending TEE to black holes with inner horizons and time-like singularities remains a daunting but essential challenge. The most pressing example is the Reissner-Nordström (RN) black hole, whose interior terminates at a time-like singularity. The key difficulty is to determine if a well-defined CWES configurations exist for such geometries, or if a completely new prescription is needed. If such extremal surfaces exist, developing a robust method to compute TEE for RN-AdS black holes would be a major step towards a universal understanding of entanglement in realistic black holes, potentially offering a new holographic tool to probe the instability of Cauchy horizons and the strong cosmic censorship conjecture.

Furthermore, our discovery that the interior causal type is linked to the existence of TEE suggests a broader conjecture. In models like holographic superconductors, matter backreaction can largely alter the asymptotic near space-like singularity geometry and produce Kasner-type chaotic behaviour [4, 5, 49, 50]. This gives a concrete setting to study how TEE responds to detailed features of the near-singularity geometry and how to detect the characteristic anisotropic oscillations (Kasner epochs) as it approaches the singularity. Beyond space-like singularities, chaotic behavior can also emerge near time-like singularities (time-like BKL interior) [51–53]. Exploring how TEE responds in such extreme scenarios represents a further test for our framework. It requires not only overcoming the challenges

of Cauchy horizons but also understanding how TEE is affected by these chaotic interior Kasner-geometries near time-like singularity.

Beyond the classification of interior phases, our results for the Schwarzschild-AdS baseline in Sec. 2 hint at another layer of universality. Previous studies on two-sided black holes have established that the HEE’s growth rate tends toward a universal constant [14, 44]. Strikingly, we observed a parallel phenomenology for TEE in the single-boundary static case. As shown in Sec. 2.4, the real part of TEE scales linearly at large boundary temporal width, $\tau_0 \rightarrow \infty$. This behavior is precisely controlled by a space-like critical surface that lingers at a specific bulk radius r_c . This compelling analogy invites a natural follow-up question: does the growth rate of single-sided TEE also obey universal upper bounds analogous to those constraining HEE? Furthermore, how do fundamental physical constraints, such as energy conditions, imprint themselves on this potential bound? We leave these interesting issues for future studies.

Finally, we wish to highlight a potential connection between TEE and Renormalization Group (RG) flows. Previous studies, such as Ref. [15], investigated “Trans-IR” flows that extend into the black hole interior to probe the singularity. Since our work establishes TEE as a sensitive probe of interior structure, it offers a natural candidate to quantify these deep RG flows. Recent works [54–56] have explored various relationships between boundary entanglement, RG flows, and bulk geometry. It would be fascinating to further investigate the precise mapping between TEE as a quantum information measure and the renormalization group flow towards the spacetime singularity.

Acknowledgments

We thank Profs. Haitang Yang and Wu-zhong Guo for helpful discussions. This work is supported by the Natural Science Foundation of China under Grant No. 12375051 and Tianjin University Self-Innovation Fund Extreme Basic Research Project Grant No. 2025XJ22-0014 and 2025XJ21-0007.

A Uniqueness of the Minimal Area Configuration

In Sec. 2.2, we established that the extremal CWES configuration for the holographic dual of TEE must satisfy the Hamilton-Jacobi condition $E(v_{A_2}) - E(v_{B'_2} = v_0 - v_{A_2}) = 0$. While $v_{A_2} = v_{B'_2} = v_0 - v_{A_2}$ is a manifest solution, we present here the proof of its uniqueness.

Our strategy is to prove that $E(v_{A_2})$ (or equivalently, $H_*(v_{A_2})$ where $E = H_*^2$, defined in Eq. (2.12)) is a strictly monotonic function of v_{A_2} . If $E(v_{A_2})$ is strictly monotonic with its argument v_{A_2} , then the condition $E(v_{A_2}) = E(v_{B'_2} = v_0 - v_{A_2})$ and Eq. (2.27) can only be satisfied if $v_{A_2} = v_{B'_2} = v_0 - v_{A_2}$. To show this, we will examine the derivative dE/dv_{A_2} :

$$\frac{dE(v_{A_2})}{dv_{A_2}} = 2H_*(v_{A_2}) \frac{dH_*(v_{A_2})}{dv_{A_2}}. \quad (\text{A.1})$$

We will prove that when $H_* > 0$ we have $\frac{dH_*(v_{A_2})}{dv_{A_2}} > 0$; $H_* < 0$ we have $\frac{dH_*(v_{A_2})}{dv_{A_2}} < 0$, in other words we always have $\frac{dE(v_{A_2})}{dv_{A_2}} > 0$. From the relation Eq. (2.16), we can compute

$\mathrm{d}v_{A_2}/\mathrm{d}H_*$

$$\frac{\mathrm{d}v_{A_2}}{\mathrm{d}H_*} = \int_{r=0}^{r=\infty} \mathrm{d}r \frac{1}{D(r; H_*)^2} \frac{\partial D(r; H_*)}{\partial H_*} , \quad (\text{A.2})$$

where we have introduced

$$D(r; H_*) = r^{4-2d} X (X + H_*^2) , \quad (\text{A.3})$$

and have used the fact that the integrand is smooth everywhere, then we could interchange differentiation and integration. A direct calculation yields

$$\frac{\partial D}{\partial H_*} = \frac{4H_*^3}{r^{2d-4}} + \frac{2H_*}{r^{2d-4}} X + \frac{2H_*^5}{r^{2d-4} X} . \quad (\text{A.4})$$

We observe that each term in $\frac{\partial D}{\partial H_*}$ is strictly positive for $r > 0$, if we assume that $H_* > 0$, we will get $\frac{\partial D(r; H_*)}{\partial H_*} > 0$; if we assume that $H_* < 0$, we will get $\frac{\partial D(r; H_*)}{\partial H_*} < 0$. Consequently,

$$\begin{aligned} \frac{\mathrm{d}v_{A_2}}{\mathrm{d}H_*} &= \int_{r=0}^{r=\infty} \mathrm{d}r \frac{1}{D(r; H_*)^2} \frac{\partial D(r; H_*)}{\partial H_*} > 0 , \quad \text{for } H_* > 0 ; \\ \frac{\mathrm{d}v_{A_2}}{\mathrm{d}H_*} &= \int_{r=0}^{r=\infty} \mathrm{d}r \frac{1}{D(r; H_*)^2} \frac{\partial D(r; H_*)}{\partial H_*} < 0 , \quad \text{for } H_* < 0 . \end{aligned} \quad (\text{A.5})$$

This shows $H_*(\mathrm{d}H_*/\mathrm{d}v_{A_2}) > 0$ and then Eq. (A.1) implies $E(v_{A_2})$ is strictly increasing with respect to v_{A_2} . We then find the unique solution for $E(v_{A_2}) = E(v_{B'_2} = v_0 - v_{A_2})$ to be $v_{A_2} = v_{B'_2} = v_0 - v_{A_2}$, which means a time-symmetric “vertical” configuration $t|_{A_2} = t|_{B_2} = 0$, as illustrated in Fig. 3(b).

It rigorously confirms that $v_{A_2} = v_{B'_2} = v_0 - v_{A_2}$ is not just *an* extremum, but the *unique* one. As a double check, we also verify numerically¹⁰ that $v_{A_2}(H_*)$, thus its inverse $H_*(v_{A_2})$, is a monotonic function, as shown in Fig. 20.

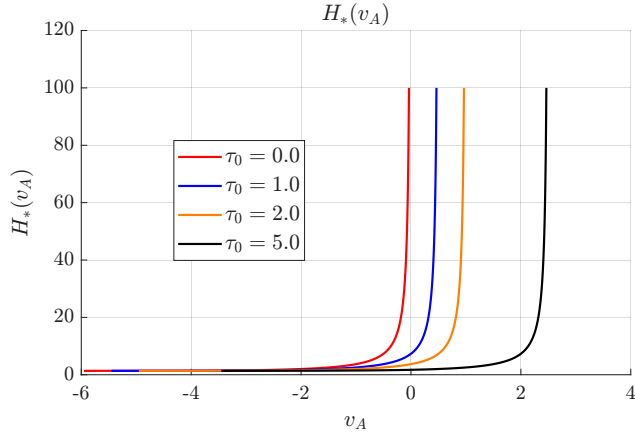


Figure 20: The numerical result suggests that $H_*(v_{A_2})$ (thus its inverse $v_{A_2}(H_*)$) is a monotonic function, where H_* varies from the lower bound (2.14) $H_{*,\min} = 2.438$ to 100.

¹⁰Here in the numerical integration of Eq. (2.16), we subtract the vacuum AdS background as in Eq. (2.32).

B Asymptotic Details of Null Limit

In this appendix, we provide a detailed derivation of the asymptotic behavior given by Eqs. (3.17) and (3.18) in the null limit, where the space-like surfaces A_1A_2 and B_1B_2 approach null surfaces, as illustrated in Fig. 18.

For the time-difference integral with metric (3.4)

$$\tau_0(H_*)/2 - v_{A_2} = \int_0^\infty \frac{dz}{e^{\chi/2} X(X + H_*^2 z^{d-1})}, \quad (\text{B.1})$$

where $X = \sqrt{H_*^4 z^{2d-2} + g e^{-\chi}}$, we could set $h^{2d-2} \equiv H_*^4$ and perform the change of variables $z = \frac{\rho}{h}$, $dz = h^{-1} d\rho$. This leads to the expression given in

$$\begin{aligned} \tau_0(H_*)/2 - v_{A_2} &= \int_0^\infty \frac{dz}{e^{\chi/2} \sqrt{H_*^4 z^{2d-2} + g e^{-\chi}} \left(\sqrt{H_*^4 z^{2d-2} + g e^{-\chi}} + H_*^2 z^{d-1} \right)} \\ &= h^{-1} \underbrace{\int_0^\infty \frac{d\rho}{e^{\chi(\rho/h)/2} \sqrt{\rho^{2d-2} + g(\rho/h) e^{-\chi(\rho/h)}} \left(\sqrt{\rho^{2d-2} + g(\rho/h) e^{-\chi(\rho/h)}} + \rho^{d-1} \right)}}_{\equiv \eta_d} \\ &= \eta_d h^{-1}, \end{aligned} \quad (\text{B.2})$$

which tells us the limit $H_* \rightarrow \infty$ corresponds to the space-like surfaces A_1A_2 and B_1B_2 approaching a null configuration. We note that above integration will be dominated by behavior of metric near AdS boundary region $z = \rho/h \rightarrow 0$ for large enough h . We then use asymptotic behaviors of the metric functions:

$$\begin{aligned} g(z) e^{-\chi(z)} &\sim 1 - \left(\frac{z}{z_h} \right)^d, & \chi(z) &= \mathcal{O}(1/z^{d+1}); \\ g(\rho/h) e^{-\chi(\rho/h)} &\sim 1 - \rho^d h^{-d} z_h^{-d}, & \chi(\rho/h) &= \mathcal{O}(\rho^{d+1}/h^{d+1}), \end{aligned} \quad (\text{B.3})$$

We then find for $d \geq 2$

$$\begin{aligned} \eta_d &= \int_0^\infty \frac{d\rho}{\sqrt{\rho^{2d-2} + 1} \left(\sqrt{\rho^{2d-2} + 1} + \rho^{d-1} \right)} \\ &= \int_0^\infty d\rho \left(1 - \frac{\rho^{d-1}}{\sqrt{\rho^{2d-2} + 1}} \right) \\ &= \frac{1}{\sqrt{\pi}} \Gamma\left(\frac{d}{2d-2}\right) \Gamma\left(\frac{2d-3}{2d-2}\right). \end{aligned} \quad (\text{B.4})$$

The individual term $\int_0^\infty 1 d\rho$ in second line diverges, but the combination above is convergent for suitable $d \geq 2$ due to cancellation at large ρ . Thus we find

$$\Delta t_{\text{UV}} = \eta_d h^{-1} + \dots. \quad (\text{B.5})$$

This gives us Eq. (3.17).

For the area integral with metric (3.4)

$$\text{Re}\mathcal{A}(H_*) = \int_0^\infty dz \frac{z^{1-d}}{e^{\chi/2} X}, \quad (\text{B.6})$$

we introduce a small cut-off parameter ϵ to regulate the near AdS boundary (UV) region $z \rightarrow 0$. We first isolate the UV-divergent contribution, splitting the integral into sub-integrals $I_1(H_*)$ and $I_2(H_*)$ as follow

$$\begin{aligned} \mathcal{A}_{A_1 A_2}(H_*) &= \int_0^\infty dz e^{-\chi/2} \frac{z^{1-d}}{\sqrt{H_*^4 z^{2d-2} + g e^{-\chi}}} \\ &= \int_\epsilon^\infty dz e^{-\chi/2} \left(\frac{z^{1-d}}{\sqrt{H_*^4 z^{2d-2} + g e^{-\chi}}} - \frac{z^{1-d}}{\sqrt{H_*^4 z^{2d-2} + 1}} + \frac{z^{1-d}}{\sqrt{H_*^4 z^{2d-2} + 1}} \right) \\ &= \underbrace{\int_\epsilon^\infty dz e^{-\chi/2} \frac{z^{1-d}}{\sqrt{H_*^4 z^{2d-2} + 1}}}_{=I_1(H_*)} + \underbrace{\int_\epsilon^\infty dz e^{-\chi/2} \left(\frac{z^{1-d}}{\sqrt{H_*^4 z^{2d-2} + g e^{-\chi}}} - \frac{z^{1-d}}{\sqrt{H_*^4 z^{2d-2} + 1}} \right)}_{=I_2(H_*)}. \end{aligned}$$

Applying the same scaling $h^{2d-2} \equiv H_*^4$ and variable change $z = \rho/h$, $dz = h^{-1}d\rho$ yields the form of sub-integral $I_1(H_*)$ for $d \geq 3$ with limit $h \rightarrow \infty$

$$\begin{aligned} I_1(H_*) &= \int_\epsilon^\infty dz \frac{z^{1-d}}{\sqrt{(h z)^{2d-2} + 1}} \\ &= h^{d-2} \int_{\epsilon h}^\infty d\rho \frac{\rho^{1-d}}{\sqrt{\rho^{2d-2} + 1}} \\ &= -\frac{h^{d-2}}{d-2} {}_2F_1\left(\frac{1}{2}, \frac{2-d}{2d-2}, \frac{d}{2d-2}, -\rho^{2d-2}\right) \rho^{-d+2} \Big|_{\epsilon h}^\infty. \end{aligned}$$

For brevity, we define the parameters of the hypergeometric function as $\alpha = 1/2$, $\beta = \frac{2-d}{2d-2}$, and $\gamma = \frac{d}{2d-2}$. We must evaluate the expression at the boundaries $\rho \rightarrow \epsilon h$ and $\rho \rightarrow \infty$. At the lower boundary $\rho = \epsilon h$, the argument of the hypergeometric function $Z = -\rho^{2d-2}$ approaches zero for $d \geq 3$. Using the expansion ${}_2F_1(\alpha, \beta, \gamma, Z) = 1 + \mathcal{O}(Z)$ as $Z \rightarrow 0$, the contribution from the lower limit is:

$$\begin{aligned} I_1(H_*)|_{\epsilon h} &= -\left(-\frac{h^{d-2}}{d-2} (\epsilon h)^{2-d} \left[1 + \mathcal{O}\left((\epsilon h)^{2d-2}\right)\right]\right) \\ &\approx \frac{\epsilon^{2-d}}{d-2}. \end{aligned}$$

Here we have supposed that $1 \gg 1/h \gg \epsilon$.

At the upper limit, the argument $Z = -\rho^{2d-2}$ diverges. To evaluate the limit, we utilize the linear transformation formula that maps $|Z| > 1$ to the region near zero:

$$\begin{aligned} {}_2F_1(\alpha, \beta, \gamma, Z) &= \frac{\Gamma(\gamma)\Gamma(\beta-\alpha)}{\Gamma(\gamma-\alpha)\Gamma(\beta)} (-Z)^{-\alpha} {}_2F_1\left(\alpha, \alpha-\gamma+1, \alpha-\beta+1, \frac{1}{Z}\right) \\ &+ \frac{\Gamma(\gamma)\Gamma(\alpha-\beta)}{\Gamma(\gamma-\beta)\Gamma(\alpha)} (-Z)^{-\beta} {}_2F_1\left(\beta, \beta-\gamma+1, \beta-\alpha+1, \frac{1}{Z}\right). \end{aligned} \quad (\text{B.7})$$

Substituting this back into the integral expression, which involves a prefactor ρ^{2-d} , we analyze the asymptotic behavior of the two terms in Eq. (B.7) as $\rho \rightarrow \infty$. For the first term in Eq. (B.7), the scaling is determined by $\rho^{2-d}(-Z)^{-\alpha} \sim \rho^{2-d}(\rho^{2d-2})^{-1/2} = \rho^{3-2d}$. For $d \geq 3$, the exponent $3-2d$ is negative, so this term vanishes as $\rho \rightarrow \infty$. For the second term in Eq. (B.7), the scaling is $\rho^{2-d}(-Z)^{-\beta} \sim \rho^{2-d}(\rho^{2d-2})^{-\frac{2-d}{2d-2}} = \rho^{2-d}\rho^{d-2} = \rho^0$. This term yields a finite constant. Consequently, only the second term in Eq. (B.7) contributes at infinity. The coefficient is calculated using $\alpha - \beta = \frac{2d-3}{2d-2}$, $\gamma - \beta = 1$. Thus, the finite contribution from the upper limit is:

$$I_1(H_*)|_\infty = -\frac{h^{d-2}}{d-2} \frac{\Gamma\left(\frac{d}{2d-2}\right) \Gamma\left(\frac{2d-3}{2d-2}\right)}{\Gamma(1)\Gamma\left(\frac{1}{2}\right)} = -\frac{\Gamma\left(\frac{d}{2d-2}\right) \Gamma\left(\frac{2d-3}{2d-2}\right)}{\sqrt{\pi}(d-2)} h^{d-2}.$$

Combining the contributions from the upper and lower limits (and the result of η_d in Eq. (B.4) for the time-difference integral), the final result for the sub-integral $I_1(H_*)$ (or $I_1(h)$) with $d \geq 3$ is

$$I_1(h) = \frac{\epsilon^{2-d}}{d-2} - h^{d-2} \frac{\eta_d}{d-2}. \quad (\text{B.8})$$

For $d = 2$, there will appear a logarithmic divergency on h :

$$\begin{aligned} I_1(H_*) &= \int_\epsilon^\infty dz \frac{z^{-1}}{\sqrt{(hz)^2 + 1}} \\ &= \int_{\epsilon h}^\infty d\rho \frac{1}{\rho \sqrt{\rho^2 + 1}} \\ &= -\ln\left(\frac{\sqrt{\rho^2 + 1} + 1}{\rho}\right)\Big|_{\epsilon h}^\infty \end{aligned}$$

At the upper limit, we have

$$I_1(H_*)|_\infty = -\ln(1) = 0.$$

The contribution from the lower limit is

$$I_1(H_*)|_{\epsilon h} = -\ln\left(\frac{\sqrt{(\epsilon h)^2 + 1} + 1}{\epsilon h}\right) = -\ln\left(\frac{2}{\epsilon h}\right).$$

Combining the contributions from the upper and lower limits, the final result for $d = 2$ is

$$I_1(h) = \ln\left(\frac{2}{\epsilon h}\right) + \mathcal{O}(\epsilon^2 h^2). \quad (\text{B.9})$$

Sub-integral $I_2(H_*)$ is treated similarly

$$\begin{aligned}
I_2(H_*) &= \int_0^\infty dz e^{-\chi(z)/2} \left(\frac{z^{1-d}}{\sqrt{H_*^4 z^{2d-2} + g(z) e^{-\chi(z)}}} - \frac{z^{1-d}}{\sqrt{H_*^4 z^{2d-2} + 1}} \right) \\
&= \int_0^\infty dz e^{-\chi(z)/2} \left(\frac{z^{1-d}}{\sqrt{(hz)^{2d-2} + g e^{-\chi}} - \sqrt{(hz)^{2d-2} + 1}} \right) \\
&= h^{d-2} \int_0^\infty d\rho e^{-\chi(\rho/h)/2} \left(\frac{\rho^{1-d}}{\sqrt{\rho^{2d-2} + g(\rho/h) e^{-\chi(\rho/h)}}} - \frac{\rho^{1-d}}{\sqrt{\rho^{2d-2} + 1}} \right) \\
&= h^{d-2} \int_0^\infty d\rho e^{-\chi(\rho/h)/2} \left(\frac{\rho^{1-d}}{\sqrt{\rho^{2d-2} + g(\rho/h) e^{-\chi(\rho/h)}}} - \frac{\rho^{1-d}}{\sqrt{\rho^{2d-2} + 1}} \right).
\end{aligned}$$

In the near AdS boundary region $z \rightarrow 0$, we use the asymptotic form Eq. (B.3) of the metric functions, which allows us to evaluate the limiting behavior of sub-integral $I_2(H_*)$ as follow

$$\begin{aligned}
I_2(H_*) &= h^{d-2} \int_0^\infty d\rho e^{-\chi(\rho/h)/2} \left(\frac{\rho^{1-d}}{\sqrt{1 + \rho^{2d-2} - \rho^d h^{-d} z_h^{-d}}} - \frac{\rho^{1-d}}{\sqrt{\rho^{2d-2} + 1}} \right) \\
&= h^{d-2} \int_0^\infty d\rho e^{-\chi(\rho/h)/2} \left(\frac{\rho^{1-d}}{\sqrt{1 + \rho^{2d-2}}} \left(1 + \frac{\rho^d h^{-d} z_h^{-d}}{2(1 + \rho^{2d-2})} \right) - \frac{\rho^{1-d}}{\sqrt{\rho^{2d-2} + 1}} \right) \\
&= \frac{h^{d-2}}{2} \int_0^\infty d\rho e^{-\chi(\rho/h)/2} \frac{\rho^{1-d}}{\sqrt{1 + \rho^{2d-2}}} \left(\frac{\rho^d h^{-d} z_h^{-d}}{1 + \rho^{2d-2}} \right) \\
&= \frac{h^{-2} z_h^{-d}}{2} \underbrace{\int_0^\infty d\rho \frac{e^{-\chi(\rho/h)/2} \rho}{(1 + \rho^{2d-2})^{3/2}}}_{\equiv \beta_d} \\
&= \frac{\beta_d}{2h^2 z_h^d}.
\end{aligned}$$

In the large- h limit, we have $e^{-\chi(\rho/h)/2} \rightarrow 1$, which allows us to read off the dimension-dependent constant β_d :

$$\begin{aligned}
\beta_d &= \int_0^\infty d\rho \frac{\rho}{(1 + \rho^{2d-2})^{3/2}} \\
&= \frac{\Gamma\left(\frac{3d-5}{2d-2}\right) \Gamma\left(\frac{1}{d-1}\right)}{\sqrt{\pi} (d-1)}.
\end{aligned} \tag{B.10}$$

Combining the results from sub-integrals $I_1(H_*)$ and $I_2(H_*)$, we obtain the complete asymptotic behavior for the area in the null limit for $d \geq 3$:

$$\mathcal{A}_{A_1 A_2}(H_*) = \frac{\beta_d}{2h^2 z_h^d} + \frac{\epsilon^{2-d}}{d-2} - h^{d-2} \frac{\eta_d}{d-2} + \dots \tag{B.11}$$

Combine it with Eq. (B.5) and we then find Eq. (3.18).

References

- [1] E.M. Lifshitz and I.M. Khalatnikov, *Investigations in relativistic cosmology*, *Adv. Phys.* **12** (1963) 185.
- [2] V.A. Belinsky, I.M. Khalatnikov and E.M. Lifshitz, *Oscillatory approach to a singular point in the relativistic cosmology*, *Adv. Phys.* **19** (1970) 525.
- [3] V.A. Belinski and I.M. Khalatnikov, *Effect of Scalar and Vector Fields on the Nature of the Cosmological Singularity*, *Sov. Phys. JETP* **36** (1973) 591.
- [4] S.A. Hartnoll, G.T. Horowitz, J. Kruthoff and J.E. Santos, *Diving into a holographic superconductor*, *SciPost Phys.* **10** (2021) 009 [[2008.12786](#)].
- [5] R.-G. Cai, L. Li and R.-Q. Yang, *No Inner-Horizon Theorem for Black Holes with Charged Scalar Hairs*, *JHEP* **03** (2021) 263 [[2009.05520](#)].
- [6] J.M. Maldacena, *The Large N limit of superconformal field theories and supergravity*, *Adv. Theor. Math. Phys.* **2** (1998) 231 [[hep-th/9711200](#)].
- [7] S.S. Gubser, I.R. Klebanov and A.M. Polyakov, *Gauge theory correlators from noncritical string theory*, *Phys. Lett. B* **428** (1998) 105 [[hep-th/9802109](#)].
- [8] E. Witten, *Anti de Sitter space and holography*, *Adv. Theor. Math. Phys.* **2** (1998) 253 [[hep-th/9802150](#)].
- [9] J.M. Maldacena, *Eternal black holes in anti-de Sitter*, *JHEP* **04** (2003) 021 [[hep-th/0106112](#)].
- [10] J. Maldacena and L. Susskind, *Cool horizons for entangled black holes*, *Fortsch. Phys.* **61** (2013) 781 [[1306.0533](#)].
- [11] S. Ryu and T. Takayanagi, *Holographic derivation of entanglement entropy from AdS/CFT*, *Phys. Rev. Lett.* **96** (2006) 181602 [[hep-th/0603001](#)].
- [12] V.E. Hubeny, M. Rangamani and T. Takayanagi, *A Covariant holographic entanglement entropy proposal*, *JHEP* **07** (2007) 062 [[0705.0016](#)].
- [13] D. Stanford and L. Susskind, *Complexity and Shock Wave Geometries*, *Phys. Rev. D* **90** (2014) 126007 [[1406.2678](#)].
- [14] T. Hartman and J. Maldacena, *Time Evolution of Entanglement Entropy from Black Hole Interiors*, *JHEP* **05** (2013) 014 [[1303.1080](#)].
- [15] E. Caceres, A. Kundu, A.K. Patra and S. Shashi, *Trans-ir flows to black hole singularities*, *Physical Review D* **106** (2022) .
- [16] L. Fidkowski, V. Hubeny, M. Kleban and S. Shenker, *The Black hole singularity in AdS / CFT*, *JHEP* **02** (2004) 014 [[hep-th/0306170](#)].
- [17] A.R. Brown, D.A. Roberts, L. Susskind, B. Swingle and Y. Zhao, *Holographic Complexity Equals Bulk Action?*, *Phys. Rev. Lett.* **116** (2016) 191301 [[1509.07876](#)].
- [18] L. Lehner, R.C. Myers, E. Poisson and R.D. Sorkin, *Gravitational action with null boundaries*, *Phys. Rev. D* **94** (2016) 084046 [[1609.00207](#)].
- [19] K. Doi, J. Harper, A. Mollabashi, T. Takayanagi and Y. Taki, *Pseudoentropy in dS/CFT and Timelike Entanglement Entropy*, *Phys. Rev. Lett.* **130** (2023) 031601 [[2210.09457](#)].
- [20] P. Wang, H. Wu and H. Yang, *Fix the dual geometries of $T\bar{T}$ deformed CFT_2 and highly excited states of CFT_2* , *Eur. Phys. J. C* **80** (2020) 1117 [[1811.07758](#)].

[21] X. Jiang, P. Wang, H. Wu and H. Yang, *Timelike entanglement entropy and $T\bar{T}$ deformation*, *Phys. Rev. D* **108** (2023) 046004 [[2302.13872](#)].

[22] K. Narayan, *de Sitter space, extremal surfaces, and time entanglement*, *Phys. Rev. D* **107** (2023) 126004 [[2210.12963](#)].

[23] Z. Li, Z.-Q. Xiao and R.-Q. Yang, *On holographic time-like entanglement entropy*, *JHEP* **04** (2023) 004 [[2211.14883](#)].

[24] K. Doi, J. Harper, A. Mollabashi, T. Takayanagi and Y. Taki, *Timelike entanglement entropy*, *JHEP* **05** (2023) 052 [[2302.11695](#)].

[25] K. Narayan, *Further remarks on de Sitter space, extremal surfaces, and time entanglement*, *Phys. Rev. D* **109** (2024) 086009 [[2310.00320](#)].

[26] X. Jiang, H. Wu and H. Yang, *Timelike entanglement entropy Revisited*, [2503.19342](#).

[27] X. Gong, W.-z. Guo and J. Xu, *Entanglement measures for causally connected subregions and holography*, [2508.05158](#).

[28] W.-z. Guo, S. He and T. Liu, *Entanglement of General Subregions in Time-Dependent States*, [2512.19955](#).

[29] W.-z. Guo, S. He and Y.-X. Zhang, *Relation between time- and spacelike entanglement entropy*, *Phys. Rev. D* **112** (2025) 086020 [[2402.00268](#)].

[30] J. Xu and W.-z. Guo, *Imaginary part of timelike entanglement entropy*, *JHEP* **02** (2025) 094 [[2410.22684](#)].

[31] J. Harper, T. Kawamoto, R. Maeda, N. Nakamura and T. Takayanagi, *Non-hermitian Density Matrices from Time-like Entanglement and Wormholes*, [2512.13800](#).

[32] C. Nunez and D. Roychowdhury, *Timelike entanglement entropy: A top-down approach*, *Phys. Rev. D* **112** (2025) 026030 [[2505.20388](#)].

[33] C. Nunez and D. Roychowdhury, *Holographic timelike entanglement across dimensions*, *JHEP* **11** (2025) 100 [[2508.13266](#)].

[34] P.-Z. He and H.-Q. Zhang, *Holographic timelike entanglement entropy from Rindler method**, *Chin. Phys. C* **48** (2024) 115113 [[2307.09803](#)].

[35] Q. Wen, M. Xu and H. Zhong, *Timelike and gravitational anomalous entanglement from the inner horizon*, *SciPost Phys.* **18** (2025) 204 [[2412.21058](#)].

[36] M. Afrasiar, J.K. Basak and D. Giataganas, *Timelike entanglement entropy and phase transitions in non-conformal theories*, *JHEP* **07** (2024) 243 [[2404.01393](#)].

[37] M. Afrasiar, J.K. Basak and D. Giataganas, *Holographic timelike entanglement entropy in non-relativistic theories*, *JHEP* **05** (2025) 205 [[2411.18514](#)].

[38] M.P. Heller, F. Ori and A. Serantes, *Geometric Interpretation of Timelike Entanglement Entropy*, *Phys. Rev. Lett.* **134** (2025) 131601 [[2408.15752](#)].

[39] W.-z. Guo and J. Xu, *Duality of Ryu-Takayanagi surfaces inside and outside the horizon*, *Phys. Rev. D* **112** (2025) L101901 [[2502.16774](#)].

[40] W.-z. Guo, *Measuring the black hole interior from the exterior*, *Int. J. Mod. Phys. D* **34** (2025) 2544006 [[2505.09878](#)].

[41] T. Anegawa and K. Tamaoka, *Black hole singularity and timelike entanglement*, *JHEP* **10** (2024) 182 [[2406.10968](#)].

[42] Y.-S. An, L. Li, F.-G. Yang and R.-Q. Yang, *Interior structure and complexity growth rate of holographic superconductor from M-theory*, *JHEP* **08** (2022) 133 [[2205.02442](#)].

[43] R. Auzzi, S. Bolognesi, E. Rabinovici, F.I. Schaposnik Massolo and G. TallaRita, *On the time dependence of holographic complexity for charged AdS black holes with scalar hair*, *JHEP* **08** (2022) 235 [[2205.03365](#)].

[44] Z. Li and R.-Q. Yang, *Upper bounds of holographic entanglement entropy growth rate for thermofield double states*, *JHEP* **10** (2022) 072 [[2205.15154](#)].

[45] D. Carmi, S. Chapman, H. Marrochio, R.C. Myers and S. Sugishita, *On the Time Dependence of Holographic Complexity*, *JHEP* **11** (2017) 188 [[1709.10184](#)].

[46] S.A. Hartnoll, C.P. Herzog and G.T. Horowitz, *Holographic Superconductors*, *JHEP* **12** (2008) 015 [[0810.1563](#)].

[47] R.-G. Cai, L. Li, L.-F. Li and R.-Q. Yang, *Introduction to Holographic Superconductor Models*, *Sci. China Phys. Mech. Astron.* **58** (2015) 060401 [[1502.00437](#)].

[48] G.T. Horowitz and M.M. Roberts, *Zero Temperature Limit of Holographic Superconductors*, *JHEP* **11** (2009) 015 [[0908.3677](#)].

[49] X.-K. Zhang, X. Zhao, Z.-Y. Nie, Y.-P. Hu and Y.-S. An, *Diving into a holographic multi-band superconductor*, *Phys. Lett. B* **868** (2025) 139684 [[2411.07693](#)].

[50] X.-K. Zhang, X. Zhao, Z.-Y. Nie, Y.-P. Hu and Y.-S. An, *Interior structure of the holographic $s+p$ superconductor and chaotic-stable transition near the black hole singularity*, *Phys. Lett. B* **872** (2026) 140110 [[2506.19419](#)].

[51] E. Shaghoulian and H. Wang, *Timelike BKL singularities and chaos in AdS/CFT*, *Class. Quant. Grav.* **33** (2016) 125020 [[1601.02599](#)].

[52] S. Bhowmick and S. Chatterjee, *Towards Timelike Singularity via AdS Dual*, *Int. J. Mod. Phys. A* **32** (2017) 1750122 [[1610.05484](#)].

[53] J. Ren, *Asymptotically AdS spacetimes with a timelike Kasner singularity*, *JHEP* **07** (2016) 112 [[1603.08004](#)].

[54] S. Grieninger, K. Ikeda and D.E. Kharzeev, *Temporal entanglement entropy as a probe of renormalization group flow*, *JHEP* **05** (2024) 030 [[2312.08534](#)].

[55] D. Roychowdhury, *Holographic timelike entanglement and c theorem for supersymmetric QFTs in $(0+1)d$* , *JHEP* **06** (2025) 003 [[2502.10797](#)].

[56] M. Afrasiar, J.K. Basak and K.-Y. Kim, *Aspects of holographic timelike entanglement entropy in black hole backgrounds*, [2512.21327](#).